HHS Public Access

Author manuscript

Int J Rock Mech Min Sci (1997). Author manuscript; available in PMC 2015 July 15.

Published in final edited form as:

Int J Rock Mech Min Sci (1997). 2013 April ; 59: 1–14.

Sequential Gaussian co-simulation of rate decline parameters of longwall gob gas ventholes

C.Özgen Karacan[a,*] and **Ricardo A. Olea**[b]

[a]NIOSH, Office of Mine Safety and Health Research, Pittsburgh, PA, United State

[b]USGS, Eastern Energy Resources, Reston, VA, United States

Abstract

Gob gas ventholes (GGVs) are used to control methane inflows into a longwall mining operation by capturing the gas within the overlying fractured strata before it enters the work environment. Using geostatistical co-simulation techniques, this paper maps the parameters of their rate decline behaviors across the study area, a longwall mine in the Northern Appalachian basin. Geostatistical gas-in-place (GIP) simulations were performed, using data from 64 exploration boreholes, and GIP data were mapped within the fractured zone of the study area. In addition, methane flowrates monitored from 10 GGVs were analyzed using decline curve analyses (DCA) techniques to determine parameters of decline rates. Surface elevation showed the most influence on methane production from GGVs and thus was used to investigate its relation with DCA parameters using correlation techniques on normal-scored data. Geostatistical analysis was pursued using sequential Gaussian co-simulation with surface elevation as the secondary variable and with DCA parameters as the primary variables. The primary DCA variables were effective percentage decline rate, rate at production start, rate at the beginning of forecast period, and production end duration. Co-simulation results were presented to visualize decline parameters at an area-wide scale. Wells located at lower elevations, i.e., at the bottom of valleys, tend to perform better in terms of their rate declines compared to those at higher elevations. These results were used to calculate drainage radii of GGVs using GIP realizations. The calculated drainage radii are close to ones predicted by pressure transient tests.

Keywords

Sequential Gaussian co-simulation; Geostatistical stochastic simulation; Longwall mining; Gob gas ventholes; Decline curve analysis; Methane control

[*]Corresponding author. Tel.: +1 412 3864008; fax: +1 412 386 6595. cok6@cdc.gov (C. Özge Karacan).

Disclaimer: The findings and conclusions in this paper are those of the authors and do not necessarily represent the views of the National Institute for Occupational Safety and Health. Mention of any company name, product, or software does not constitute endorsed by NIOSH or USGS.

Appendix A. Supporting information

Supplementary data associated with this article can be found in the online version at http://dx.doi.org/10.1016/j.ijrmms.2012.11.003.

1. Introduction

Drilling gob gas ventholes (GGVs) in longwall mining panels is a common technique to control methane emissions, allowing for the capture of methane within the overlying fractured strata before it enters the work environment during mining. The usual practice is to drill the GGVs prior to mining and locate a slotted casing in the zone that is expected to fracture (fractured zone). As mining advances under the venthole, the strata that surround the well deform and establish preferential pathways for the released methane, mostly from the coal seams within the fractured zone, to flow towards the ventholes [1]. The properties of fractured zones, mainly permeability, are determined through conventional pressure- and rate-transient well test analyses techniques that are used systematically and routinely for oil and gas [2–6]. Results showed that permeabilities of bedding plane separations can be as high as 150 Darcies, with average permeabilities (including fractures and intact formations) within the slotted casing interval of GGVs varying between 1 Darcy and 10 Darcies [7–9].

GGVs are equipped with exhausters on the surface to provide negative pressure to produce methane from highly permeable fractured zones with a rate and concentration depending on various additional factors besides permeability [10–11]. The production life-span of GGVs may be long or short, depending on mining, borehole drilling, and location as well as operating conditions, but usually follows a declining trend with time [8] until the exhausters are shut down as a safety measure against explosion risk, when the methane concentration in the produced gas decreases to approximately 25%.

It is difficult to predict production performance of GGVs due to the involvement of multiple factors [10,12]. In addition to complexities given in these studies, boreholes may deform under mining stresses and strata displacements [13–15], making production predictions even more difficult. Studies presented in [7,12] do not take borehole stability issues into account while predicting GGV performance. However, Karacan [10] presented a sensitivity analysis of variables on total flow rate and methane percentage of gas produced from GGVs. The sensitivity analyses showed that, when considering the overall performance of GGVs for methane production rate, the most important variables were 1, whether or not face is advancing, 2, surface elevation of the venthole (above sea level), 3, overburden, 4, casing diameter, 5, distance of the venthole to the tailgate, and 6, distance of venthole to panel start.

Multiple factors studied in [10] and then improved in [11] were formulated as a multi-layer-perceptron (MLP) type neural network to predict GGV production performance. This module is part of MCP 2.0-Methane Control and Prediction software, v.2 [16] for prediction and sensitivity analyses purposes. Version 1.3 of this software is briefly discussed [17].

Despite the improvements for understanding the effects of various factors on GGV production and for predicting GGV performance, there are GGVs that perform much better or worse than expected in terms of methane production rate and production longevity. Although these unexpected production behaviors may be due to borehole stability issues, as mentioned before, they can also be related to spatial location of the borehole and how it interacts with other important production-influencing factors at that particular position. In other words, if there is a spatial correlation or stochastic dependency between borehole

location, its rate transient, and other potentially influencing factors, the analyses should involve the geographical location of the boreholes, necessitating geostatistical methods.

Geostatistical methods, some of which are described in detail in [18–22], have wide applications in geology, environmental studies, mining research, and petroleum engineering [23–28]. More recently, Olea et al. [29] have developed a formulation of a correlated variables methodology and co-simulation for assessment of gas resources in Woodford shale play, Arkoma basin, in eastern Oklahoma.

The aim of this paper is to explore the possibility of modeling the attributes of decline curve analyses (DCA) conducted on gob gas ventholes by taking into account borehole locations and potential correlations between surface elevations at the wellheads. Geostatistical stochastic co-simulation methods were used to map the distribution of decline curve attributes. In addition, cell-based DCA parameters were interpreted with the GIP in the fractured zone to estimate radii of drainage area of GGVs.

2. Site location and description of area in relation to correlations with gob gas venthole production

The longwall mining site studied in this paper is in the Pittsburgh coal, Monongahela Group, southwestern Pennsylvania. The Monongahela Group includes sandstone, siltstone, shale and commercial coal beds and occurs from the base of the Pittsburgh coal bed to the base of the Waynesburg coal bed. Thickness within the general study area ranges from 270 to 400 ft. The Pittsburgh coal seam is unusually continuous and covers more than 5000 square miles [30], making longwall mining technique highly suitable in this region.

Mining the Pittsburgh seam creates a gas emission zone that extends from the Pittsburgh Rider to Waynesburg coal beds (Fig. 1), spanning to a height of ~350 ft [31]. However, in the gas emission zone, Sewickley, Uniontown and Waynesburg coal beds are the main coal seams that occur within the fractured zone (~ 80–350 ft from the top of the Pittsburgh seam). During mining, these coal seams are fractured vertically and horizontally and their methane is liberated into the fracture system. The methane emissions from these coals are believed to be the main source of gas from the fractured zone, which is controlled by drilling GGVs from the surface in advance of mining. A simplified stratigraphy of the studied region, a schematic of a GGV and its drilling distance, the specific panel area where modeling was conducted, and the monitored GGV locations are shown in Fig. 1.

The GGVs shown in red in Fig. 1 were monitored for flowrates, methane percentage in produced gas, and pressures at the well head. GGVs shown in blue marks were equipped with downhole transducers by the field personnel to monitor the change in head of water initially filled in the boreholes. This information was used to calculate hydraulic conductivities as a function of face location. Data collected at the surface for flow and pressures were later used for decline curve analyses.

In southwest Pennsylvania, the topography consists of frequent hills and valleys, which control underground fracture networks, flow of groundwater, and the presence of gas.

Fractures are usually within the valleys and are generally stress-relief fractures that were generated during erosional events [32]. Fracture patterns are vertical, parallel to the valleys and situated in valley floors.

Wyrick and Borchers [33] reported that groundwater flow associated with stress relief fractures occurs in the valley bottoms and valley sides. Therefore, wells in the valleys are more likely to produce high water yields. This fracturing is expected to diminish beneath the adjacent hills, thereby limiting the effective areal extent and yield of aquifers [32]. Subsidence caused by longwall mining results in tension and compression of the near-surface zone, increasing or decreasing the fracture transmissibility, especially in valley bottoms, suggesting that GGVs drilled in the valleys may be more productive [33]. Based on an earlier integrated study evaluating hydraulic properties of underground strata and their potential responses to longwall mining, Karacan and Goodman [34] concluded that GGVs drilled in the valleys might be more productive than those drilled on hilltops. They also observed that the borehole location affected fracturing during dynamic subsidence in such a way that hilltop GGVs seemed to fracture earlier than valley-bottom wells. However, the permeability of the fractures at the hilltop wells was less compared to that of valley-bottom wells due to greater overburden thickness.

Wells at higher elevations, and thus with greater overburden thickness for a nearly flat coal bed such as the Pittsburgh seam, usually cause lower hydraulic conductivities and potentially less effective GGVs as opposed to shallow overburden wells. Thus, less overburden and lower surface elevations correlate better with GGV production. These observations and monitoring results are in agreement with Fig. 1 in terms of the influence of surface elevation on methane production from GGVs, and are the basis for selecting surface elevation as the secondary variable, as discussed in forthcoming sections.

3. Decline curve analyses of gob gas venthole data

3.1. Production data and analyses methodology

Decline curve analysis is a rate transient test procedure used for analyzing declining production rates and forecasting future performance of wells. In this paper, Fekete's rate transient analysis (RTA) [35] software was used to analyze declining GGV production performances using both traditional decline approaches and Fetkovich type curves.

In decline curve analysis, it is implicitly assumed that the factors causing the historical decline continue unchanged during the forecast period. These factors include both reservoir conditions and operating conditions of the borehole. As long as these conditions do not change, the trend in decline can be analyzed and extrapolated to forecast future well performance [35,36]. This implicit assumption can be especially valid for gob reservoirs after the mining face passes the GGV location by at least several hundreds of feet or after completion of the panel. At these stages, caving and subsidence are complete at a particular GGV location, and no further major reservoir changes are expected. Under constant percentage or exponential decline conditions, plots of log-rate vs. time and rate vs. cumulative production should both result in straight lines from which the decline rate can be determined.

An example of traditional DCA with fitted data of GGV-1 shown in Fig. 1 is given in Fig. 2. This figure shows the GGV-1 production data analyzed with an exponential decline curve using gas rate vs. time and gas rate vs. cumulative production plots. Some important data that can be drawn from these analyses relating to production and forecast intervals, as well as their locations, are shown schematically in Fig. 3. These parameters and their acronyms, shown in Fig. 3 caption, will be used as primary variables in co-simulations and will be referred to frequently in this paper.

The relationship of various parameters in exponential decline analysis are given below for decline coefficient and cumulative production between two time intervals, respectively, from the acronyms used in Fig. 3 and its caption:

$$\ln\left(\frac{QFC}{QP}\right) = -PD \times FC$$

$$CUM.P = \frac{QP}{PD}\{1 - \exp[-PD(FC - TP)]\}$$

Cumulative productions at different production times can be obtained by changing the FC to the desired time in Eq. (2).

3.2. Results of production decline analyses of GGVs

Table 1 shows the descriptive statistics of the DCA results of methane production data. The DCA allowed for the determination of eight attributes derived from the production of 10 GGVs. These results show that percentage decline of the GGVs ranges from 47 to 100%/year, with a mean of 78%/year. Table 1 further shows that the rate of methane production at the start of the GGVs' production life, just after interception with longwall face, can vary between low values (~2 Mscf/day) and higher ones (336Mscf/ day). However, the production can cease at rates between 2 Mscf/ day and 217 Mscf/day (rate at forecast start period) and the GGVs can be short-lived (23 days) or longer (348.3 days), as observed from forecast-start time. Depending on their production characteristics, GGVs can capture cumulative methane between 3 MMscf and 102 MMscf, out of expected ultimate recovery (EUR) values ranging from 5 MMscf to 172 MMscf. These values correspond to a methane capture efficiency varying from ~2% to ~60% considering only the minimum and maximums of EURs. Thus, there are significant differences among the performance of the GGVs that were drilled in this area.

Ten observations for each DCA attribute are too few to establish a meaningful histogram for assessing the distributions of the DCA parameters across the study area and for selecting which ones could be used as primary variables.

4. Surface elevation data and modeling of gas-in-place in fractured zone

The mining district modeled in this work (Fig. 1) hosted Pittsburgh seam panels 1250 ft wide initially (the first two panels), with wider panels (1450 ft) starting from the 3rd panel.

Panel lengths were generally 12,000–13,000 ft in length. The dimensions of the area shown in Fig. 1 are 8624 ft in the y-direction (Northing) and 17,325 ft in the x-direction (Easting). In this district, overburden depths ranged between 700 and 1000 ft. This area was modeled in a 100 × 50 (Easting-Northing) Cartesian grid in which each cell was 175 ft in the x-direction and 176 ft in the y-direction.

Surface elevation of the study area was obtained from U.S. Geological Survey seamless data warehouse [37] digitally and used as the secondary variable. The original digital resolution of the surface elevation map of the study area was 30 ft × 30 ft as it was extracted from the database. However, in order for it to match exactly to the grid model of the study area and to the GGV locations, the high-resolution data was scaled up to the number of cells and to the cell dimensions of the model grid using averaging with bi-linear interpolation. Thus, the final surface elevation map was the same as the above. Fig. 4 shows the up-scaled map, which was generated for use in GIP calculations and as the secondary variable in co-simulations.

Fig. 5 shows the histogram of surface elevation data in Fig. 6. Basic statistics in this histogram, based on the values of 5000 cells, gives a minimum elevation of 932.3 ft, a maximum elevation of 1384.5 ft, a mean elevation of 1083.6 ft, and a standard deviation of 87.9 ft.

The data used in geostatistical modeling of gas-in-place (GIP) were obtained from 63 vertical exploration boreholes drilled over the mining area shown in Fig. 6. Because the top of the fractured zone for these mines was 350 ft from the top of the Pittsburgh coal [31], the data beyond this interval were excluded from further analyses. For each coal seam of interest in the fractured zone (Sewickley, Uniontown and Waynesburg seams), two attributes were determined at the spatial locations of each of the exploration boreholes for geostatistical modeling of GIP: overburden depth and coal thickness. Overburden depths were calculated by subtracting the sea-level elevation of each of the coal seams from the surface elevation data at those particular locations. Results of univariate statistical analyses of coal seam attributes are given in Table 2.

GIP simulations, whose modeling and computational procedure was developed and documented in detail for a different field in an earlier paper [38] and will not be repeated here for this district, were still pursued as an independent attribute. The univariate data given in Table 2 and the spatial distributions of these data based on the exploration boreholes shown in Fig. 8 are used for geostatistical modeling of GIP. However, GIP has not been used as a secondary variable in co-simulations simply because surface elevations are measured and provide more accurate data. In addition, surface elevation was found to be one of the most influential parameters on GGV production rates and their declines [10]. Nevertheless, GIP data still add value in analyzing performance of GGVs and thus they were used to compare cumulative productions from GGVs and to set approximate drainage areas for GGVs after co-simulations.

4.1. Semivariogram modeling of surface elevation and of GIP attributes

For sequential Gaussian simulation and co-simulation techniques to be applicable, the data should follow a Gaussian (normal) distribution. Therefore, the surface elevation and attributes of coals (depth and thickness) were transformed to normal scores by targeting a Gaussian distribution with a mean of *0* and variance of 1 [20–21]. The semivariograms were modeled on the normal-score data, and later were transformed back to the original space during simulations by targeting their original distributions. The Stanford University Geostatistical Modeling Software (SGeMS) was used for semivariogram analyses and for geostatistical simulations [20]. The semivariograms were modeled according to the guidelines provided in [39] and by studying the directional experimental semivariograms of normal scores. Experimental semivariograms were searched at 0°, 45°, 90°, and 135° starting from north and changing towards the east direction of lag vectors. In addition, an omni-directional semivariogram was modeled. Simulations, though, were performed with the omni-directional semivariograms of each attribute since anisotropy was not detected.

Fig. 7 shows the experimental semivariogram for the normal-score data of Sewickley coal seam depth and surface elevation as examples of the attributes modeled in this study. The analytical semivariogram models of the variables for the three coal seams that were used in GIP calculations are summarized in Table 3.

4.2. Sequential Gaussian simulation of GIP

Sequential Gaussian simulation (SGSIM) is a semivariogram-based simulation technique that generates simulated results, or so-called realizations, of the attribute in question by extracting the spatial patterns from the input data and semivariograms. Realizations can be seen as numerical models of possible distributions of the simulated property in space. In practice, these realizations take the form of a finite number of simulated maps equally probable to represent the unknown true map. Therefore, each grid in each of these realizations, or simulated maps, generates a distribution of the particular attribute. These distributions can be used to analyze the data statistically for variances and to evaluate the uncertainty associated with various values in a probabilistic fashion. It should be mentioned that ordinary kriging and co-kriging could have been used instead of simulation for spatial modeling. However, kriging causes severe smoothing effect on the results and also simulation is more suited to evaluate uncertainty [38]. In addition, Heriawan and Koike [40] compared two spatial models of coal quality by ordinary kriging and sequential Gaussian simulation, and clarified the merits using the simulation.

In this work, 100 realizations for each attribute of interest for GIP calculations were generated. For verification of the statistical accuracy of these realizations, the results of sequential Gaussian simulations of modeled attributes (thickness and overburden depth) were compared with the original data before proceeding with calculations of GIP and the associated uncertainties. These comparisons required *Q*–*Q* plots of hard data (measured data) along with SGSIM realizations. *Q*–*Q* plots (not shown here but readers are referred to [38] for an example) gave acceptable linear trends between hard data and realizations, indicating that the probability distributions of these two datasets are almost the same, and

SGSIM produces representative simulated distributions of probability distributions of actual data.

After the representativeness of these realizations for the raw attribute data were checked using *Q–Q* plots, GIP computations were performed for each of the three coal seams, which later were summed to compute the GIP maps of the fractured zone. One hundred realizations of GIP of the fractured zone for the area shown in Fig. 1 were generated.

The simulation results distributed in each of the realizations can be used for statistical evaluations of uncertainty using the histograms. For instance, the values of GIP for the fractured zone can be calculated at 5%, 50%, and 95% quantiles (Q5, Q50, Q95). These quantiles represent the ranking of the estimated attribute, where each estimated value has the 5th, 50th, and 95th place in ranking analyses. In other words, the estimated values of 5%, 50%, and 95% have a probability to be lower than the actual unknown value. Among these, Q50 represent the median of the possible population distribution for the calculated variables.

The cell values within each of the 100 realizations and percentile analyses were conducted to extract the realizations that correspond to Q5, Q50, and Q95 of fractured zone GIP. The GIP results shows that cumulative GIP in this area ranges between 3550 MMscf (3.55 Bscf) and 4150 MMscf (4.15 Bscf). These values are important as they state that, assuming GGVs produce methane only from the GIP in the fractured zone, the cumulative production from all boreholes combined cannot exceed 4.15 Bscf.

Fig. 8 shows the histograms of cell values (5000 cells) of GIP for Q5, Q50, and Q95, whose basic statistics are given in Table 4. This figure and table show that the GIP values in realizations corresponding to Q5, Q50, and Q95 are distributed within a minimum and maximum range of ~0.24 MMscf/cell and ~1.5 MMscf/cell, respectively, with a mean of ~0.75 MMscf/cell. These values correspond to ~0.34 MMscf/acre, ~2.05 MMscf/acre, and ~1.1 MMscf/acre, as minimum, maximum, and mean, respectively. However, it is also noteworthy that the histograms given in Fig. 8 show bimodal distributions, which indicate the existence of two distinct zones of GIP within the study area. GIP maps corresponding to Q5, Q50, and Q95 (Fig. 9) show that the western portion of the study area has potentially more GIP in the fractured zone then the eastern portion. Therefore, methane control and ventilation requirements will be different in these two areas.

5. Selection of primary variables and co-simulations

5.1. Selection of primary variables

In this paper, the potential of geostatistics to model decline curve attributes of a limited number of GGVs is sought by utilizing the location of wells and by considering the correlation potential of DCA attributes with surface elevation of wells. For this purpose, surface elevation data shown in Fig. 4 are used as the secondary variable in co-simulations.

The next step was to identify which DCA parameters could be selected as primary variables of co-simulations. In order to determine these variables, a correlation analysis between all possible DCA parameters and surface elevation was conducted using the normal scores of all attributes. The results of this analysis are given in Table 5. In selecting the primary

variables based on the correlation coefficients, the objective was to select the meaningful primary variables that have reasonably high correlations with the secondary variable. Moreover, two variables having an absolute correlation coefficient larger than 0.9 were judged dependent upon each other. This excluded the variable RR that had a larger correlation coefficient with the surface elevation than the variables QFC and QP, for instance. Additional effort was also made to avoid selecting primary variables that will repeat themselves in co-simulations. Moreover, selected variables should have enabled derivation of others using their relations through exponential decline relations given in Eqs. (1) and (2). Therefore, methane rate at production start (QP), percent decline (PD), end of possible production period (END), and production rate at start of forecast period (QFC) were selected as primary variables to be simulated with surface elevation (ELEV).

5.2. Sequential Gaussian co-simulations of primary variables with secondary variables

Different implementations of sequential simulations in SGeMS can be used for different purposes [20,29]. For this work, sequential Gaussian co-simulation with Markov-model-1 (MM1) was selected. The absence of need to generate cross-correlation, while still maintaining the ability to produce realistic results [29,41], is an advantage of this method in the face of especially limited data points.

Sequential Gaussian co-simulation allows for simulation of a Gaussian variable while accounting for the secondary information to which it correlates [20]. Due to the nature of the simulation method, the variables should either be Gaussian or should be transformed to normal scores. The latter was followed in the study since the variables were not Gaussian.

MM1 considers the following Markov-type screening hypothesis during simulations: the dependence of the secondary variable on the primary is limited to the co-located primary variable. The cross-covariance is then proportional to the auto-covariance of the primary variable [20], which can be shown as

$$C_{12}(\mathbf{h})=\frac{C_{12}(0)}{C_{11}(0)}C_{11}(\mathbf{h})$$

where **h** is the distance vector, C_{12} is the cross covariance between the two variables, and C_{11} is the covariance of primary variable. Thus, solving the co-kriging algorithm with MM1 requires the knowledge of correlation between primary and secondary variables, as well as the semivariogram(s) of the primary variable(s). These requirements, as implemented in the face of limited amount of data for primary variables, were addressed by determining the range of correlation coefficients instead of using a single value. For this purpose, a Monte Carlo (MC) routine using multi-normal correlation based on Cholesky decomposition was implemented. The routine generated 1000 normal-score data for each of the primary DCA variables and the surface elevation by using their normal-score means and standard deviations. This procedure, implemented for each of the four primary-secondary variable pairs selected, generated a range of correlation coefficients that were normally distributed around the 10-data value. These 1000 values were reduced to 100 by random sampling and were used for running 100 realizations by varying the correlation coefficient in each co-

simulation run. The correlation coefficient distributions for each primary-secondary variable pair are given in Fig. 10.

Semivariogram of primary variable based on limited data locations was approximated by the semivariogram of the secondary variable in normal-score space as all attributes in normal-score space have sills of 1, regardless of the attribute being modeled. Therefore, the sill of the semivariogram for surface elevation is the same as the sill of the “unknown” semivariogram of the primary variable. This is especially true if the primary and the secondary variables are correlated. This implies that the semivariogram ranges and nuggets must be quite similar too. Of course, it can be argued that correlation coefficients based on 10 wells are in the order of ~0.7 and thus nugget and ranges may not be exactly the same. This argument is partly taken care of by generating a range of correlation coefficients around the mean that will reflect on results and is also supported by the influence of surface elevation on production and decline characteristics discussed in [10,34]. Thus, as continuation of the above approach approximating the parameters of the primary semivariogram, the same shape of the secondary semivariogram, which is given in Fig. 7B, was used as the primary semivariogram. As the last step in simulation methodology, the normal-score primary attributes generated from co-simulations were back-transformed into real-space values.

6. Results and discussion

6.1. Co-simulated realizations of primary variables using cell-based evaluation

Co-simulations using the MM1 approach were performed to generate 100 realizations for each of the primary variables. The realizations of DCA parameters co-simulated with surface elevation shown in Fig. 4 can be used in a variety of ways to improve the understanding of rate decline properties of GGVs drilled at different locations. One of the most useful applications of all 100 realizations from each of the parameters is to calculate local probability above certain thresholds. With this application, local probability at each cell location can be calculated using the threshold value and the local cumulative probability distribution from 100 values. The results are presented as probability maps. In this study, the median values of each of the co-simulated DCA parameters were selected as the threshold value for local probability calculations. The median values were 77.8%/year for PD, 787.8 days for END, 0.106 MMscf/day for QFC, and 0.163 MMscf/day for QP. The maps that show the local probabilities for these four DCA parameters to have values above their medians are shown in Fig. 11A–D.

The local probability maps were generated based on 100 values in each of the 5000 cells and, comparing these with the surface elevation map given in Fig. 6, show general areas where GGVs perform above the set threshold values (medians). These figures show that the probability of percentage decline being larger than 77.8%/year is greater at high elevations (Fig. 11A) and that the GGVs drilled at or close to hilltops can have very high decline rates over time and may not produce for long enough periods to extract an incremental amount of methane. This is also confirmed with the probability map given in Fig. 11B, which indicates that hilltop wells have very little probability producing with extended periods of time (exceeding ~788 days). These maps show that only the GGVs drilled at the lowest

elevations have high probabilities of having slower decline rates and extended production lives.

Fig. 11C and D shows the probabilities of having methane production rates at certain stages of GGV production. For instance, Fig. 11C shows the local probabilities that GGVs will still produce with methane rates more than 0.106 MMscf/day at the start of the forecast period. This figure shows that the probabilities for this are higher only for GGVs drilled in the valleys. Fig. 11D shows the probabilities of GGVs producing with methane rates higher than 0.163 MMscf/day at the very start of the production life. This figure shows that the probabilities of such rates can only be possible if the GGVs are located in the valleys; the probability decreases towards the hillsides and becomes almost zero at the hilltops.

The probability maps prove two important observations with regard to the decline properties of GGVs: (a) GGVs drilled at or close to hilltops have higher rates of decline and are shorter lived and (b) wells drilled at hilltops start producing methane at lower rates compared to their counterparts drilled in the valleys. They also have higher rates when the GGVs eventually enter the forecast period, which means that even though these GGVs may have rates sufficient to sustain production, they can cease production due to other problems that high overburden can create such as lower fracture permeabilities and larger strains on the wellbore that may promote casing failure. In fact, [34] showed that calculated hydraulic conductivities in GGV-11 to GGV-15 shown in Fig. 1 decreased at higher overburden depths as the longwall face was approaching.

6.2. Quantile estimates of co-simulated results

The histograms of co-simulation results for PD, END, QFC and QP were used to determine the realizations at Q5, median (Q50), and Q95 of simulated attributes using ranking analyses. Distribution of cell values of these realizations with corresponding quantiles are shown in Fig. 12A – D for co-simulated DCA variables.

Table 6 shows the summary statistics of the data given in Fig. 12. In this table, DCA parameters that correspond to Q50 values were shaded since Q50 will be used in further analyses of GGV performances in combination with GIP realizations. The results given in this table are based on analyses of 5000 cell values from realizations, but they generally are in accord with the values obtained from 10 GGVs and given in Table 1. Differences in some of the values—ranges and standard deviations in particular— compared to their counterparts given in Table 1 are due to quantile ranking, mostly because the co-simulated values are spread closer to normal distribution.

6.3. Integrating co-simulation results of DCA with decline functions for performance prediction

Fig. 13 shows the realizations that correspond to 50% quantile (Q50) for each of the co-simulated parameters. The values in each cell in these DCA attribute maps can be considered as the values that a GGV will have if drilled at any given cell, with the provision that only some of these 5000 drill-location choices (cells) can actually be drilled. With this in mind, the maps in Fig. 13 show that in the majority of the region, especially where the surface elevations are high, the GGV would have very high decline rates (> 80%/year). Only

in the regions where there are valleys would the GGVs have decline rates in the 50–70%/year range. In addition, these high decline rates would be associated with lower methane production rates at the start of GGV production. The values presented based on the Q50 maps of DCA attributes in Fig. 13 are in agreement with the local probabilities calculated for each cell (Fig. 11) and the interpretation offered in Section 6.1.

The spatial DCA data given as maps not only can be used to generate synthetic decline curve analysis test data for selected locations but can also be used to predict performance of any GGV that can be drilled at any random location on the terrain by use of decline functions. As an example of this application, the virtual GGVs shown in Fig. 14 were created and located randomly at various locations on the surface elevation map to cover a range of surface elevations and locations on the terrain, such as valleys, hillsides and hilltops. By using the DCA maps from co-simulations as the decline parameters of these GGVs, and by using Eq. 2 as the expression for cumulative production in exponentially declining wells at any given time, realizations of cumulative methane productions were created. These calculations were performed by replacing FC (forecast start time) term in Eq. 2 with desired times; 30, 60, 120, 180, and 240 days, in this case. Then, a ranking analysis was performed on the results to find the realizations that corresponded to various quantiles, using the same procedure described in Section 6.2 to find various quantiles of DCA simulations. To finish the prediction for cumulative methane productions, the data at the exact locations of the virtual GGVs were extracted. These data from Q50 realizations of 30, 60, 90, 120, 180, and 240 days are given in Fig. 15.

Fig. 15 shows that the GGVs had differing production performances based on the DCA data that these GGVs acquired at their locations. The cumulative production data predicted for various production times showed that the GGVs located at the highest elevations, such as hilltops (E, F, G, I, K), had generally the lowest amount of cumulative methane production. On the other hand, the GGVs located at the lowest elevations (C, D, H, J, L), such as valleys and lower edge of the hills, had the highest cumulative methane productions. The difference in cumulative production between best and worst performing GGVs at the end of 240 days was about 15 MMscf of methane.

6.4. Integrating performance prediction based on DCA maps with GIP results to estimate drainage area

GGVs, as with other boreholes in any reservoir, should be drilled with a well-planning protocol to determine where and how many wellbores should be drilled in a given region by considering surface and reservoir conditions. This includes paying attention to any possible interference between GGVs. The results presented in the previous section can be integrated with GIP maps (Fig. 9) to estimate possible drainage radii of GGVs in the fractured zone and potential for interference due to overlapping drainage zones.

In order to demonstrate the drainage radius estimation for GGVs, the same virtual GGVs shown in Fig. 14 and their performance results given in Fig. 15 were used. These results were also combined with the GIP maps given in Fig. 9. The GIP amounts at the exact same cells as the virtual GGVs are shown in Fig. 16 for Q5, Q50, and Q95. This figure shows that GIP is lowest at A, C, and D locations and the amount is ~0.4 MMscf/cell. GIP is highest at

B, E, F, I, K, and L. These are primarily the locations towards the west and south of the model area. GIP amount in these locations is between 0.8 and 1.2 MMscf/cell range.

Estimation of the drainage radii of GGVs starts with evaluating cumulative methane production of GGVs at any given time. For this purpose, cumulative production data for 30 days and 240 days at 50% quantile (Q50) given in Fig. 15 were used, as well as the Q50 values of the GIP at given locations from Fig. 16. Knowing the size of each cell, the cumulative production amount, and the GIP corresponding to each location, the drainage radius of each GGV can be calculated. However, this calculation is based on the assumption that all GIP will be produced from the GGV and surrounding cells, i.e., recovery efficiency is 100%. Based on this procedure, the estimated drainage radii of each GGV are given in Fig. 17 as a function of surface elevation at virtual GGV locations. This figure shows that drainage radii can change between 200 and 400 ft at only 30 days of production of GGVs, whereas they increase to values between 500 ft and 1000 ft, depending on the location and the GIP values, after 240 days of production. If different methane extraction efficiency is taken into account, the estimated radii will change accordingly. Also, it is clearly seen from this plot that drainage radii decrease with increase in surface elevation of the GGV location. This is in agreement with the impact of surface elevation on DCA parameters discussed earlier in this paper and in [10].

Radii values estimated in this section compare favorably with the ones predicted from pressure transient tests. Karacan [7] predicted radii of investigations for operating GGVs as 578 and 2818 ft, depending on the locations, by use of pressure transient analyses of multi-rate drawdown test techniques. The results given in this paper also compare, within the order of magnitude, with the radius of investigation (~4000 ft) of a well in a completely different setting and known to produce from a bedding-plane separation [9] in a bounded gob reservoir.

The differences in production behaviors and rate transient (decline) behaviors of gob gas ventholes, along with their radii of investigations, can be attributed to various factors as discussed previously. Surface elevation of drill locations can have significant correlations with rate transient behaviors of these wells. Analyses reveal that the better performing wells are usually at lower elevations (and lower overburden depths) compared to poorly performing ones. Therefore, locations of the GGVs should be selected with care. This can be attributed to higher fracture permeability and shorter casing length for the exhauster to pull the methane, as opposed to tighter fractures below hilltops and longer casings. Therefore, if the GGVs have to be drilled at hilltops, it is advisable to drill them at closer spacings due to the smaller radius of drainage that was proven in this study and in earlier studies. The drainage radii can also be estimated using DCA and GIP predictions, which will give better design criteria when considered together. Along these lines, geostatistical simulation and co-simulation techniques can be used as advanced tools as part of the planning and to assess uncertainty in making the decisions related to drilling locations and prediction of rate declines of the GGVs.

Here we have simulated all four primary variables by correlating them to the same secondary variable. A challenge for the future that should yield additional improvements

would be the simultaneous simulation of all five attributes. In addition, a rock fracture network model of gob and geostatistical implementation of fractures to compare and improve accuracy of the findings of simulation of DCA parameters will be highly valuable. Such models can show the paths of fluid flow through rock fractures [42,43] and improve the understanding on DCA parameters.

7. Summary and conclusions

In this paper, geostatistical analysis was pursued using sequential Gaussian co-simulation to characterize decline curve analyses (DCA) of gob gas ventholes in combination with GIP in fractured zone and surface elevation. Surface elevation was selected as the secondary variable, while various attributes of DCA were treated as primary variables. GIP was also simulated with sequential Gaussian technique, used in conjunction with decline curve results to determine the drainage radii and production quantities.

The results obtained from this study evaluated important attributes of methane capture from mining environments, such as gob gas venthole production rates, decline rates, production ending durations, and cumulative gas productions. Employing sequential Gaussian simulation and co-simulation enabled not only the estimation of important parameters of DCA that have correlations with surface elevations but also the assessment of their uncertainty and values at certain quantiles of statistical evaluation.

This study showed that GGVs can have very high decline rates for a majority of the modeled mining district. In addition, these high decline rates were associated with lower production rates at the start of production and consequently less cumulative production. Geostatistical simulation results were used to calculate drainage radii of GGVs using GIP realizations. This work showed that the calculated drainage radii were close to ones predicted by pressure transient tests. Therefore, geostatistical analyses along with co-simulations of DCA and GIP and surface elevation data could be used to estimate the rate transient parameters and drainage radii of the wellbores, thus aiding designers in both placement and spacing of the GGVs.

Although the general belief in the coal region of the Northern Appalachian Basin is that gas production is improved by drilling GGVs at the margins of the tailgate in the longwall panel, this study showed that surface elevation might be an important consideration as well. Therefore, it is important to select the locations of the GGVs with care. In general, wells located at lower elevations, i.e., at the bottom of valleys, tended to perform better in terms of their rate declines compared to those at higher elevations. Thus, it is advisable to drill GGVs with closer spacing at hilltops due to their smaller radii of investigations.

In conclusion, geostatistical simulation and co-simulation techniques can be used as advanced tools as part of the planning process and to assess uncertainty in making decisions related to drilling locations and prediction of rate declines of the GGVs.

Conversion table (English to SI units)

1 ft = 0.3048 m

$1\ ft^2 = 22.957 \times 10^{-6}$ acre

1 MMscf = 28316 m^3

1 scfm = 0.0004719 m^3/s

Supplementary Material

Refer to Web version on PubMed Central for supplementary material.

Acknowledgments

We are grateful for the reviews as part of the internal approval process by our institutions: Gerrit Goodman on the NIOSH side, and Leslie F. Ruppert (USGS) and Michael Ed. Hohn (West Virginia Geological and Economic Survey) for the U.S. Geological Survey. We also thank Chris Garrity (U.S. Geological Survey) for providing the high-resolution surface elevation data.

References

1. Karacan CÖ, Esterhuizen GS, Schatzel S, Diamond WP. Reservoir-simulation based modeling for characterizing longwall methane emissions and gob gas venthole production. Int J Coal Geol. 2007; 71:225–245.
2. Nashawi IS. Pressure transient analysis of infinite-conductivity fractured wells producing at high flow rates. J Petrol Sci Eng. 2008; 63:73–83.
3. Sheng JJ. A new technique to determine horizontal and vertical permeabilities from the time-delayed response of a vertical interference test. Transp Porous Media. 2009; 77:507–527.
4. Escobar FH, Ibagon OE, Montealegre MM. Average reservoir pressure determination for homogeneous and naturally fractured formations from multi-rate testing with the TDS technique. J Petrol Sci Eng. 2007; 99:204–212.
5. King GR, Ertekin T, Schwerer FC. Numerical simulation of the transient behavior of coal-seam degasification wells. SPE Form Eval. 1986:165–183.
6. Kuchuk FJ, Onur M. Estimating permeability distribution from 3 D interval pressure transient tests. J Petrol Sci Eng. 2003; 39:5–27.
7. Karacan CÖ. Reconciling longwall gob gas reservoirs and venthole production performances using multiple rate drawdown well test analysis. Int J Coal Geol. 2009; 80:181–195.
8. Dougherty HN, Karacan CÖ, Goodman GVR. Reservoir diagnosis of longwall gobs through drawdown tests and decline curve analyses of gob gas venthole productions. Int J Rock Mech Min Sci. 2010; 47:851–857.
9. Karacan CÖ, Goodman GVR. Monte Carlo simulation and well testing applied in evaluating reservoir properties in a deforming longwall overburden. Transp Porous Media. 2011; 86:415–434.
10. Karacan CÖ. Forecasting gob gas venthole production performances using intelligent computing methods for optimum methane control in longwall coal mines. Int J Coal Geol. 2009; 79:131–144.
11. Karacan CÖ, Luxbacher KD. Stochastic modeling of gob gas venthole production performances in active and completed longwall coal mines. Int J Coal Geol. 2010; 84:125–140.
12. Lunarzewski LW. Gas emission prediction and recovery in underground coal mines. Int J Coal Geol. 1998; 35:117–145.
13. Whittles DN, Lowndes IS, Kingmana SW, Yates C, Jobling S. Influence of geotechnical factors on gas flow experienced in a UK longwall coal mine panel. Int J Rock Mech Min Sci. 2006; 43:369–387.
14. Whittles DN, Lowndes IS, Kingman SW, Jobling Yates CS. The stability of methane capture boreholes around a long wall coal panel. Int J Coal Geol. 2007; 71:313–328.
15. Karacan CÖ, Ruiz FA, Cote M, Phipps S. Coal mine methane: a review of capture and utilization practices with benefits to mining safety and to greenhouse gas reduction. Int J Coal Geol. 2011; 86:121–156.

16. Karacan, CÖ. Methane control and prediction (MCP) software (version 2.0). 2010. <http://www.cdc.gov/niosh/mining/products/product180.htm>
17. Dougherty HN, Karacan CÖ. A new methane control and prediction software suite for longwall mines. Comput Geosci. 2011; 37:1490–1500.
18. Deutsch, CV.; Journel, AG. GSLIB Geostatistical software library and user's guide. 2nd edition. New York: Oxford University Press; 1998.
19. Gómez-Hernández, JJ.; Cassiraga, EF. Theory and practice of sequential simulation. In: Armstrong, M.; Dowd, PA., editors. Geostatistical simulation. Dordrecht: Kluwer; 1994. p. 111-124.
20. Remy, N.; Boucher, A.; Wu, J. Applied geostatistics with SGeMS, a user's guide. Cambridge: Cambridge University Press; 2009.
21. Olea, RA. A Practical primer on geostatistics. U.S. Department of the Interior. U.S. Geological Survey, Open-File Report 2009-1103; 2009.
22. Wackernagel, H. Multivariate geostatistics—an introduction with applications. 3rd edition. Berlin: Springer; 2010.
23. Hohn ME, Neal DW. Geostatistical analysis of gas potential in Devonian shales of West Virginia. Comput Geosci. 1986; 12:611–617.
24. Watson WD, Ruppert LF, Bragg LJ, Tewalt SJ. A geostatistical approach to predicting sulfur content in the Pittsburgh coal bed. Int J Coal Geol. 2001; 48:1–22.
25. Carroll ZL, Oliver MA. Exploring the spatial relations between soil physical properties and apparent electrical conductivity. Geoderma. 2005; 128:354–374.
26. Heriawan MN, Koike L. Identifying spatial heterogeneity of coal resource quality in a multilayer coal deposit by multivariate geostatistics. Int J Coal Geol. 2008; 73:307–330.
27. Hindistan MA, Tercan AE, Unver B. Geostatistical coal quality control in longwall mining. Int J Coal Geol. 2010; 81:139–150.
28. Olea RA, Luppens JA, Tewalt SJ. Methodology for quantifying uncertainty in coal assessments with an application to a Texas lignite deposit. Int J Coal Geol. 2011; 85:78–90.
29. Olea RA, Houseknecht DW, Garrity CP, Cook TA. Formulation of a correlated variables methodology for assessment of continuous gas resources with application to the Woodford play, Arkoma Basin, eastern Oklahoma. Bol Geol Min. 2011; 122:483–496.
30. Tewalt, SJ.; Ruppert, LF.; Bragg, LJ.; Carlton, RW.; Brezinski, DK.; Wallack, RN.; Butler, DT. 2000 Resource assessment of selected coal beds and zones in the Northern and Central Appalachian Basin Coal Regions, by the Northern and Central Appalachian Basin Coal Regions Assessment Team. U.S. Geological Survey Professional Paper 1625-C; 2001. p. 101[Chapter C].
31. Karacan, CÖ. Goodman GVR Probabilistic modeling using bivariate normal distributions for identification of flow and displacement intervals in longwall overburden. Int J Rock Mech Min Sci. 2011; 48:27–41.
32. Stoner, J.; Williams, DR.; Buckwalter, TF.; Felbinger, JK.; Pattison, KL. Water resources and the effects of coal mining, Greene County, Pennsylvania. Pennsylvania: Water Resource Report 63; 1987.
33. Wyrick, GG.; Borchers, JW. Hydrologic effects of stress relief fracturing in an Appalachian valley. Washington DC: US Department of the Interior, US Geological Survey, Water Supply Paper 2177; 1981.
34. Karacan CÖ, Goodman GVR. Hydraulic conductivity changes and influencing factors in longwall overburden determined by slug tests in gob gas ventholes. Int J Rock Mech Min Sci. 2009; 46:1162–1174.
35. Fekete Associates. F.A.S.T. RTA. Advanced rate transient analysis. Calgary, Alberta: 2010. <http://www.fekete.com/software/rta/description.asp>
36. Dake, LP. Fundamentals of reservoir engineering. Amsterdam: Elsevier; 1978.
37. USGS. Seamless Data Warehouse. Data available from U.S. Geological Survey, Earth Resources Observation and Science (EROS) Center, Sioux Falls, SD. 2011. <http://seamless.usgs.gov/faq_listing.php?id=1>

38. Karacan CÖ, Olea RA, Goodman GVR. Geostatistical modeling of gas emission zone and its in-place gas content for Pittsburgh seam mines using sequential Gaussian simulations. Int J Coal Geol. 2012; 90–91:50–71.
39. Olea RA. A six-step practical approach to semivariogram modeling. Stochastic Environ Res Risk Assess. 2006; 20:307–318.
40. Heriawan MN, Koike K. Uncertainty assessment of coal tonnage by spatial modeling of seam distribution and coal quality. Int J Coal Geol. 2008; 76:217–226.
41. Karacan, CÖ. Goodman GVR Analyses of geological and hydrodynamic controls on methane emissions experienced in a Lower Kittanning coal mine. Int J Coal Geol. 2012; 98:110–127.
42. Xu C, Dowd P. A new computer code for discrete fracture network modeling. Comput Geosci. 2010; 36:292–301.
43. Koike K, Sanga T. Incorporation of fracture directions into 3D geostatistical methods for a rock fracture system. Environ Earth Sci. 2012; 66:1403–1414.

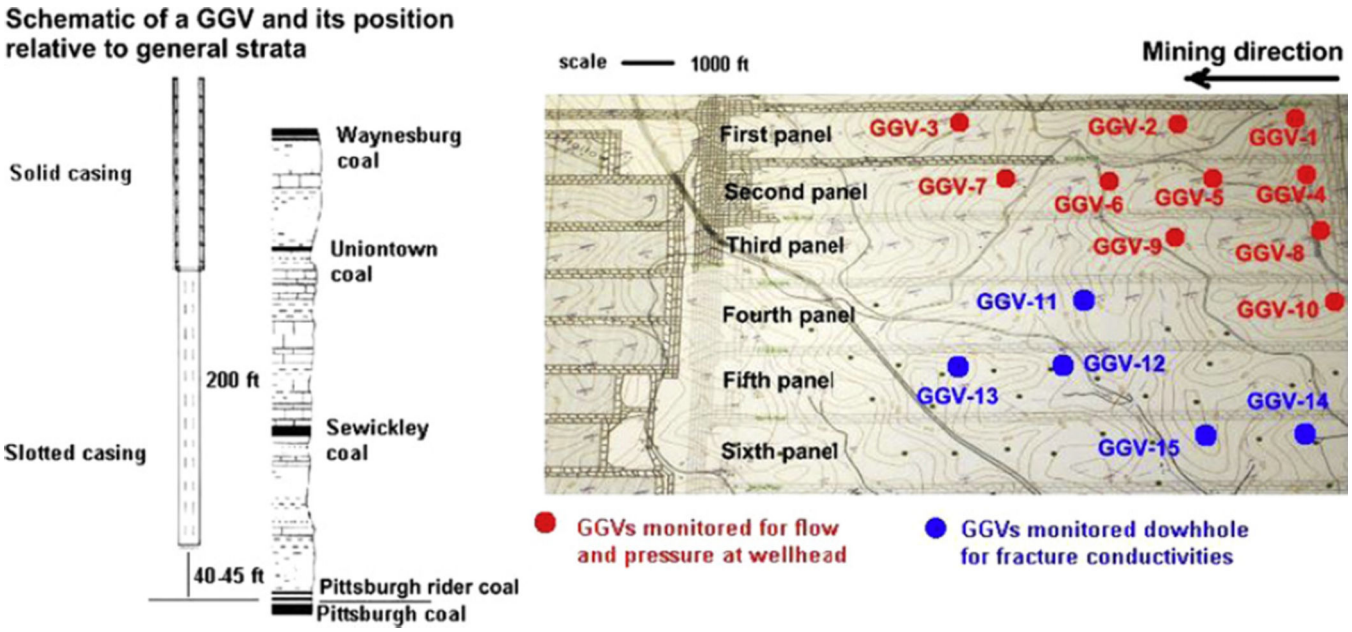

Fig. 1.

Schematic representation of stratigraphy and completion of the gob gas ventholes (GGVs), as well as panels and locations of the GGVs, in the study area. The dimensions of the area shown in this figure are 8624 ft in the *y*-direction and 17,325 ft in the *x*-direction. (For interpretation of the references to color in this figure caption, the reader is referred to the web version of this article.)

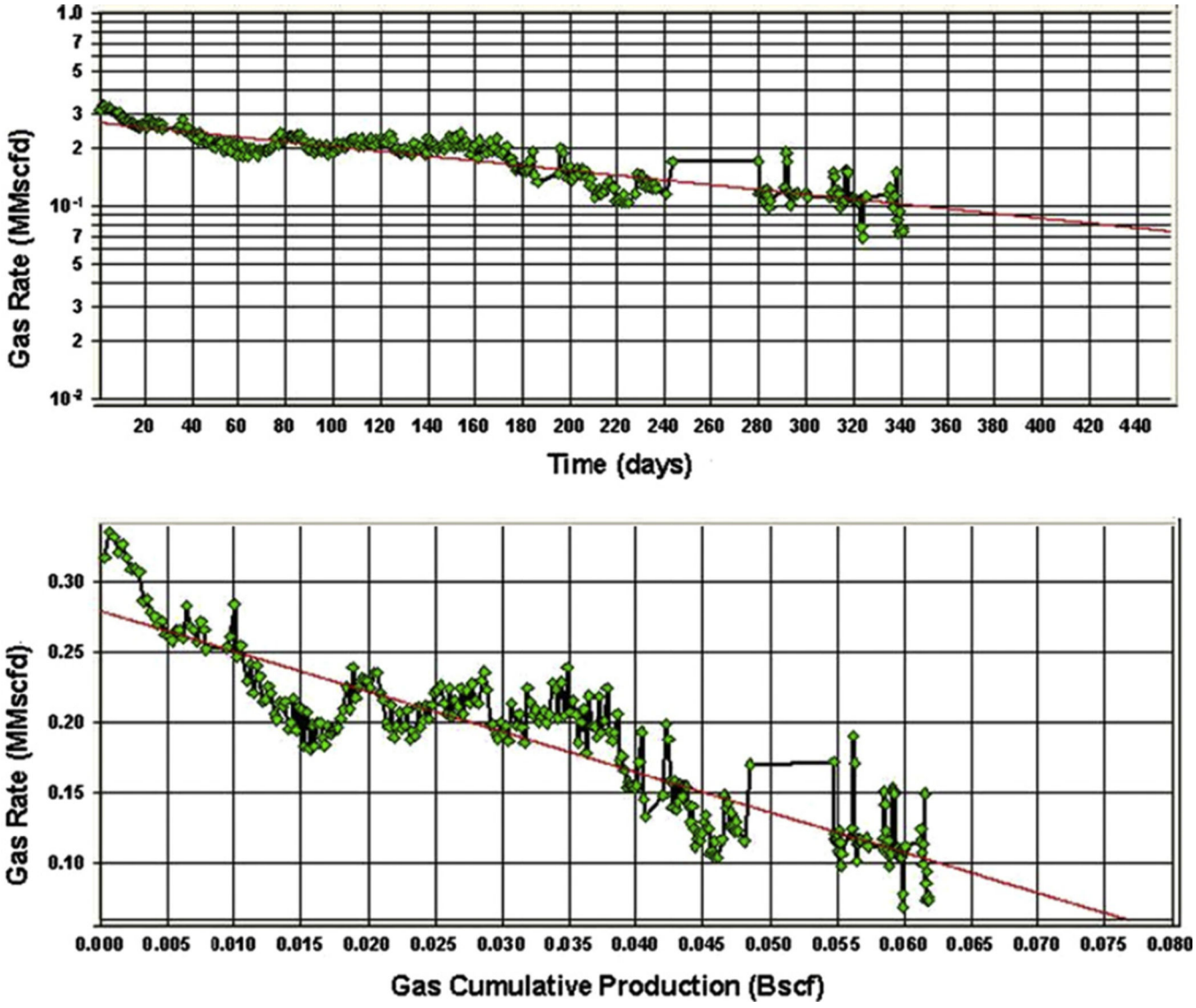

Fig. 2.

Traditional DCS with exponential decline curve (red line) of methane production data (green circles) from GGV-1 (Fig. 1). (For interpretation of the references to color in this figure caption, the reader is referred to the web version of this article.)

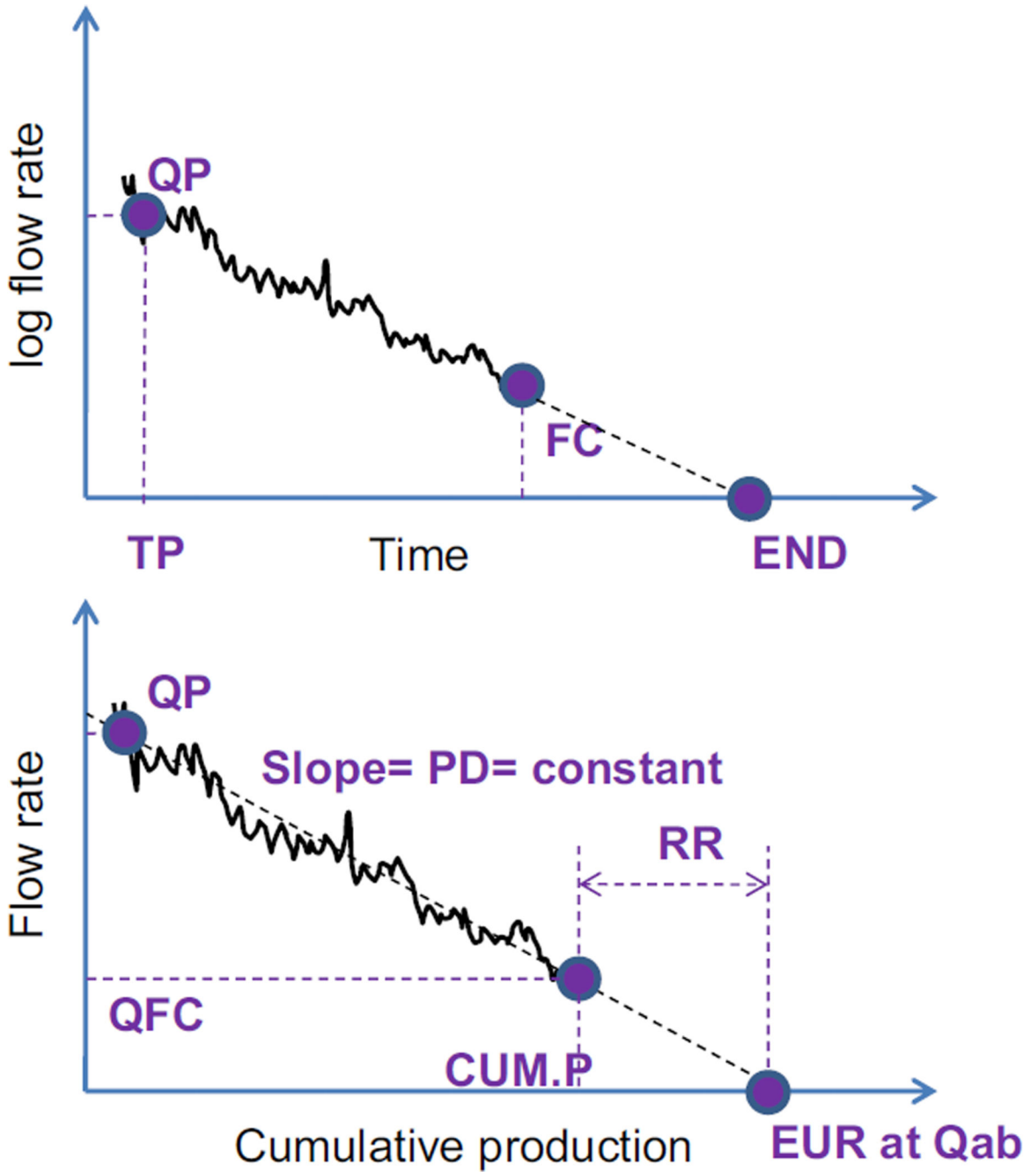

Fig. 3.

Schematic representation of rate parameters and important times in exponential decline analysis. In this plot, QP, initial production rate; TP, production start time; FC, forecast start time; END, end of the potential production life of the well; PD, percentage decline (constant decline rate); QFC, rate at forecast start; CUM.P, cumulative production till forecast start; RR, recoverable reserves; EUR, expected ultimate recovery; Qab, abandonment rate.

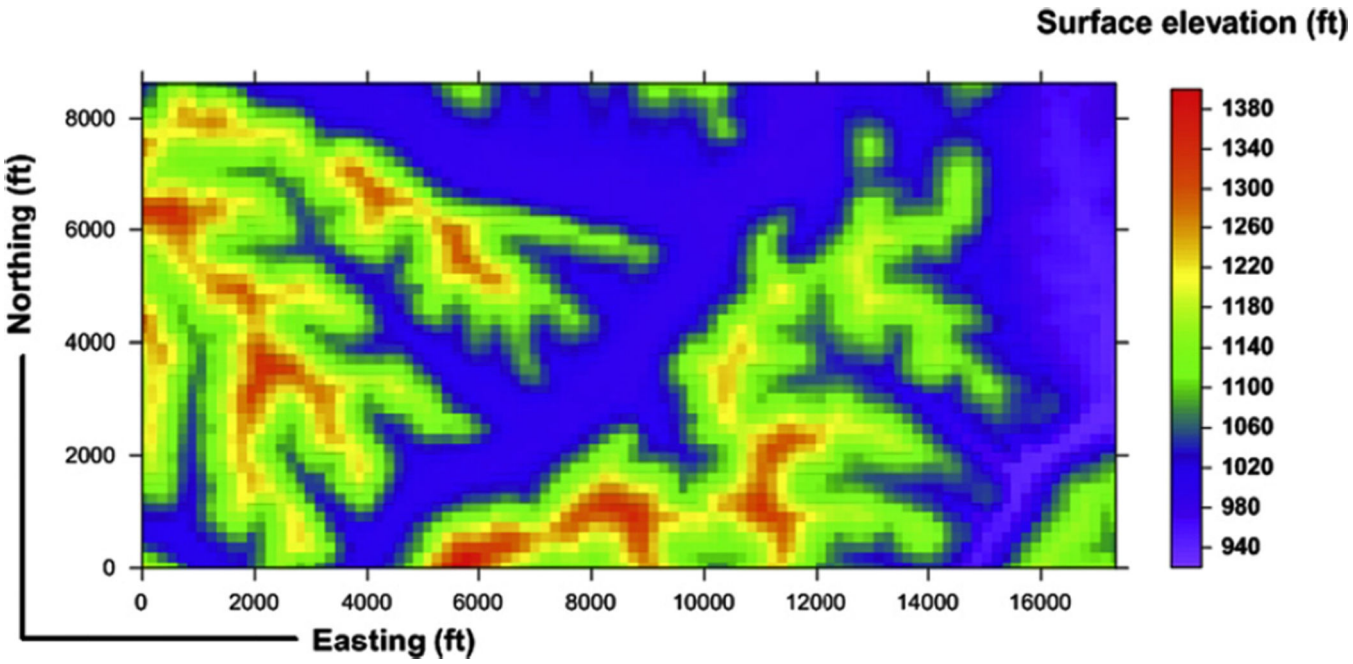

Fig. 4.

Surface elevation map at 175 ft × 176 ft resolution after up scaling the high resolution map at 30 ft × 30 ft resolution.

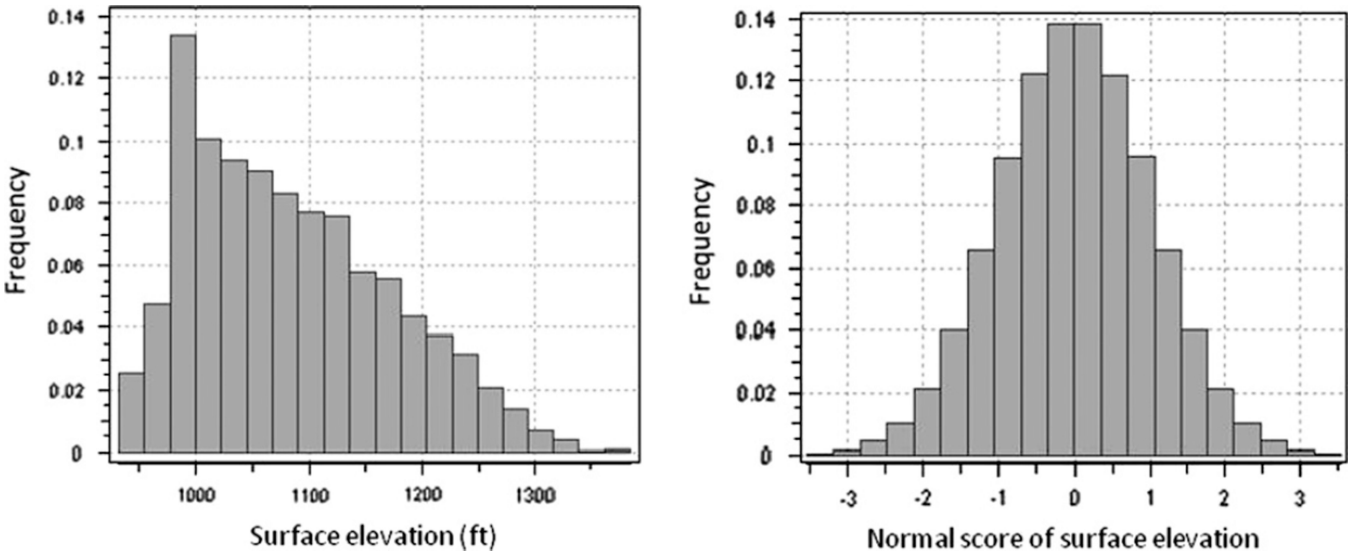

Fig. 5.
Histograms of the surface elevation data shown in Fig. 4 and its normal score distribution.

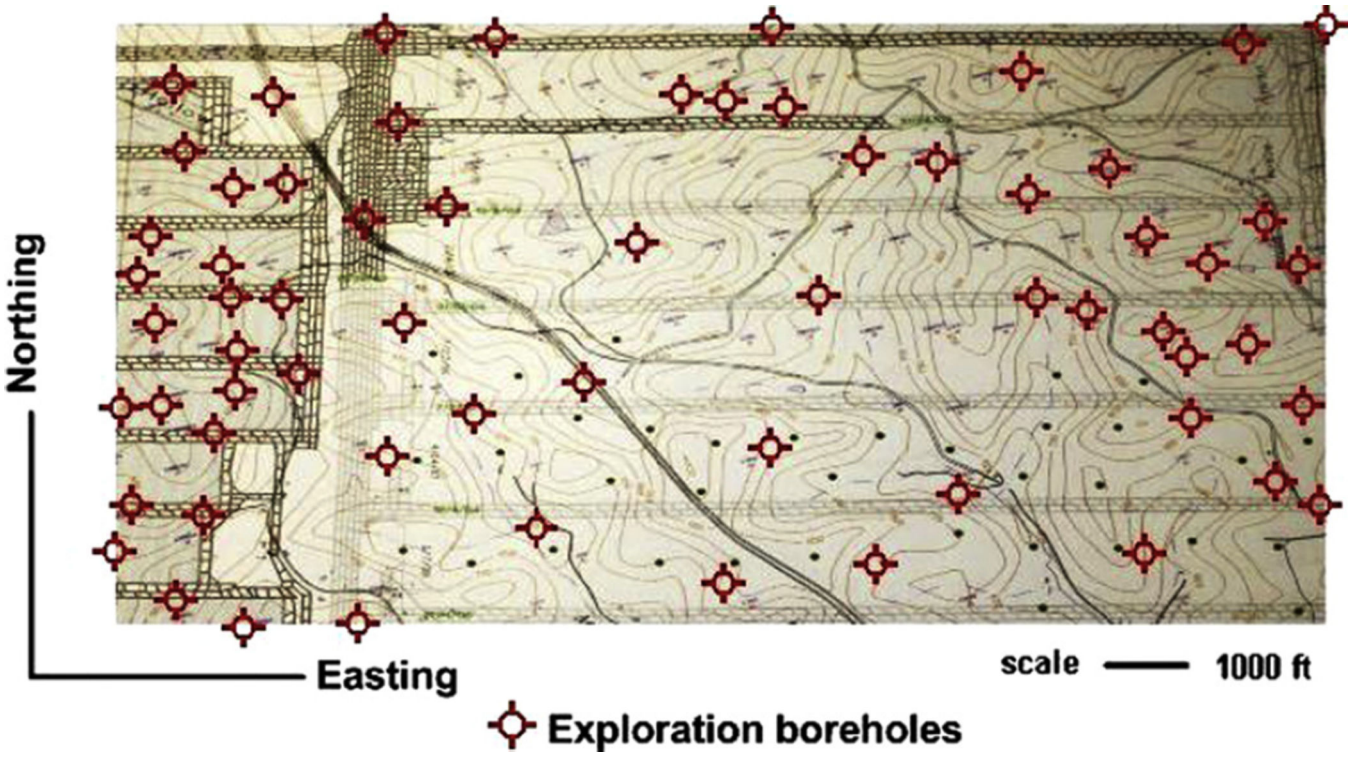

Fig. 6.
Spatial locations of the exploration boreholes drilled over the area shown in Fig. 1.

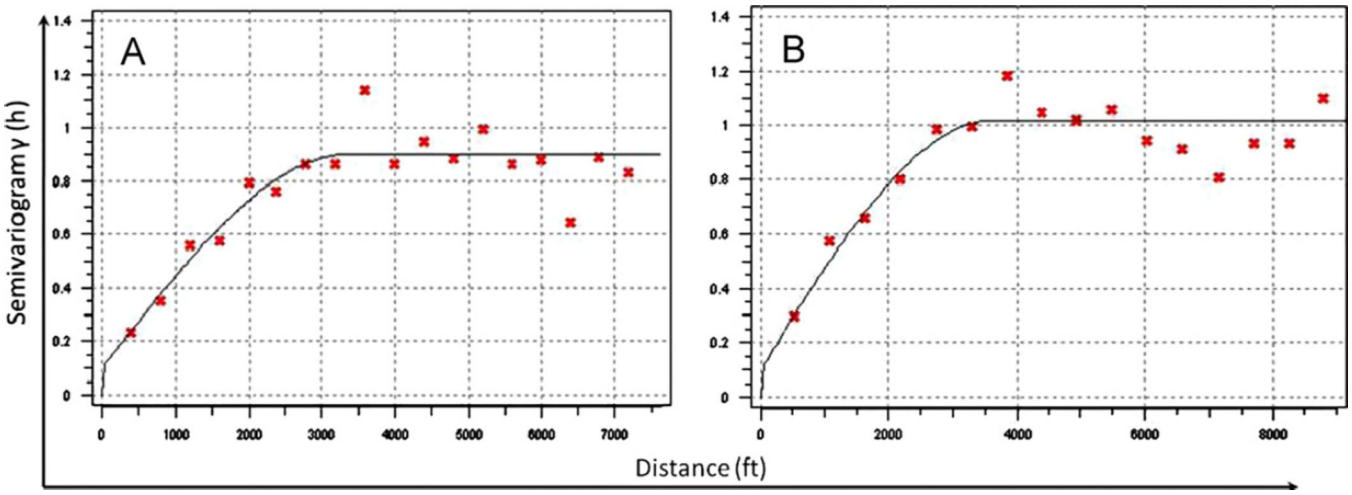

Fig. 7.

Omni-directional experimental semivariograms of normal scores of Sewickley seam depth (A) and surface elevation (B) (red crosses), and the spherical analytical semivariograms modeling them (black line). (For interpretation of the references to color in this figure caption, the reader is referred to the web version of this article.)

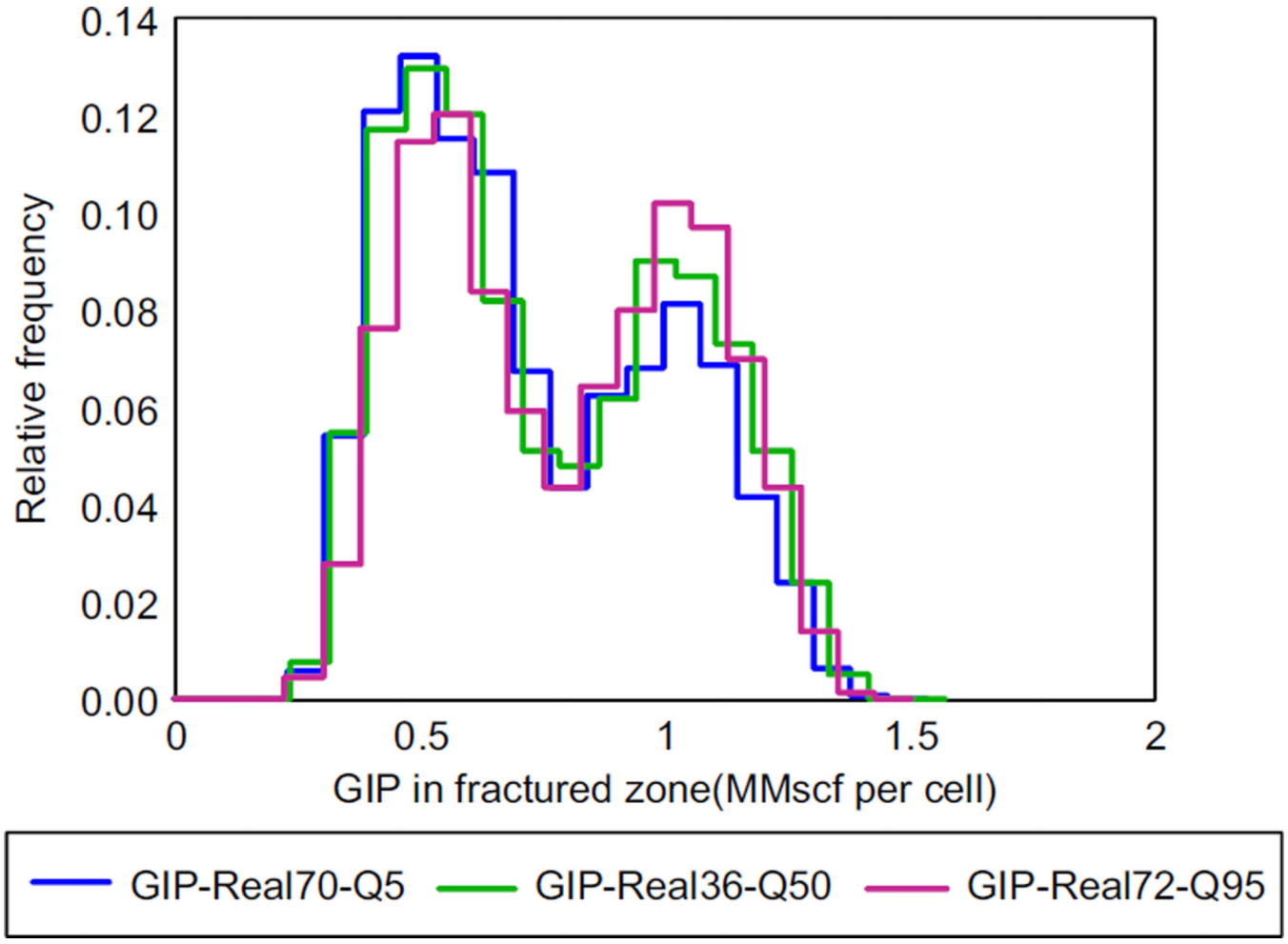

Fig. 8.

Distributions of fractured zone GIP in realizations corresponding to quantiles Q5, Q50 and Q95 (Real stands for realization in the legend).

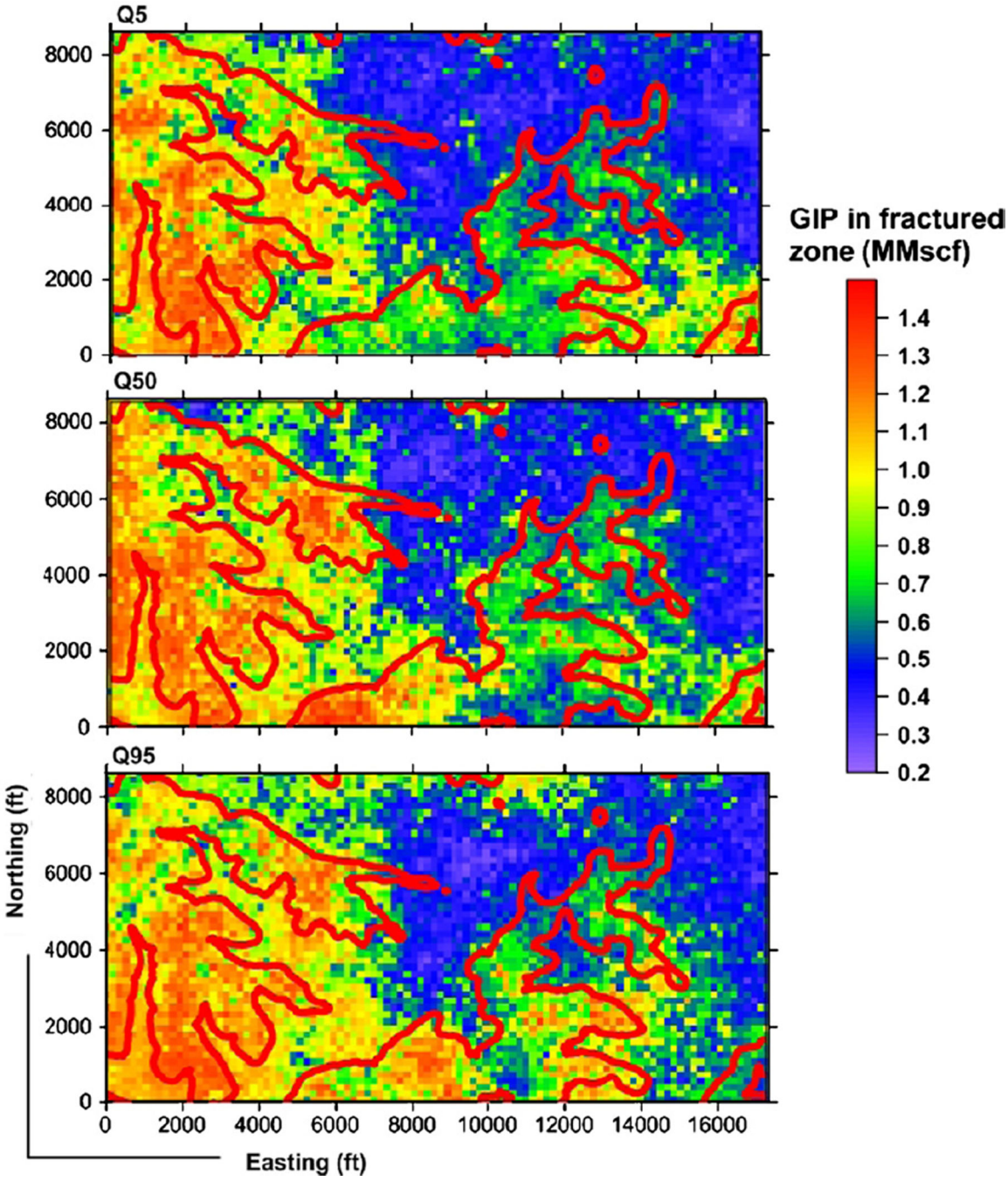

Fig. 9.

Q5, Q50, and Q95 realizations of GIP in the fractured zone of the study area shown in Fig. 1. The red line is the 1100-ft contour of surface elevation to show the edge of hills. (For interpretation of the references to color in this figure caption, the reader is referred to the web version of this article.)

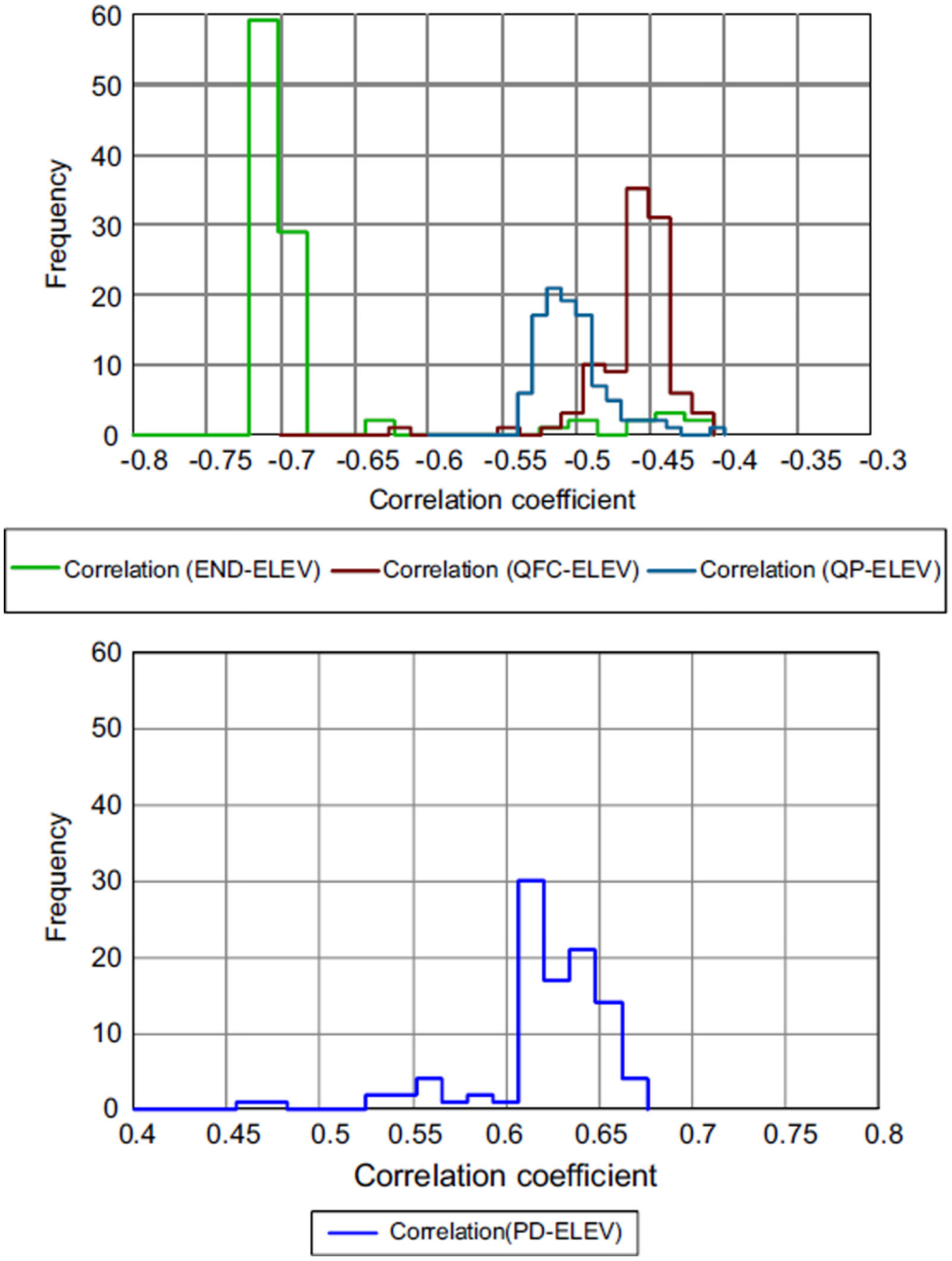

Fig. 10.
Range of correlation coefficients generated for each of the primary-secondary variable pairs to be used in co-simulations.

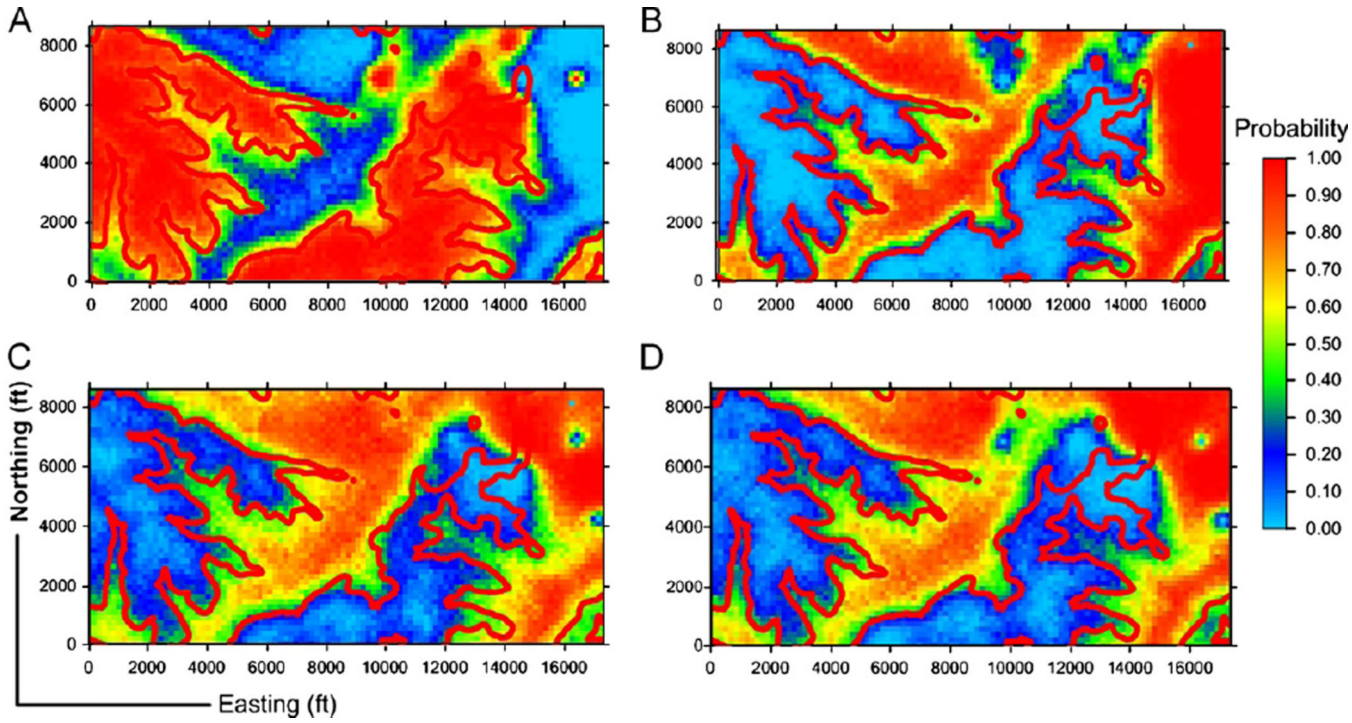

Fig. 11.

Maps that show the local probabilities for DCA parameters for values above their medians. The red line is the 1100-ft surface elevation contour. (For interpretation of the references to color in this figure caption, the reader is referred to the web version of this article.)

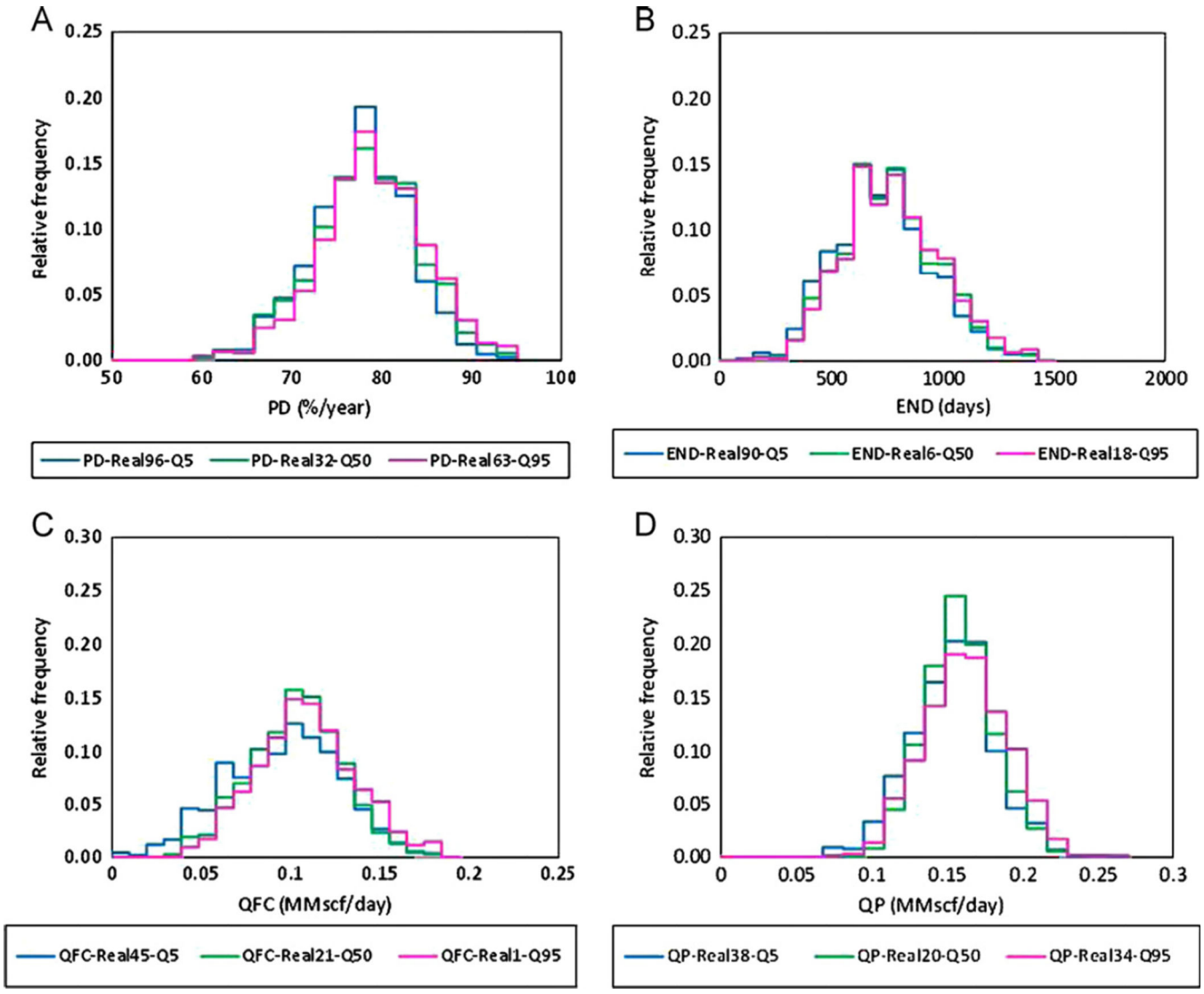

Fig. 12.

Histograms of cell values in realizations corresponding to Q5, Q50, and Q95 of DCA parameters (real stands for realization in the legends).

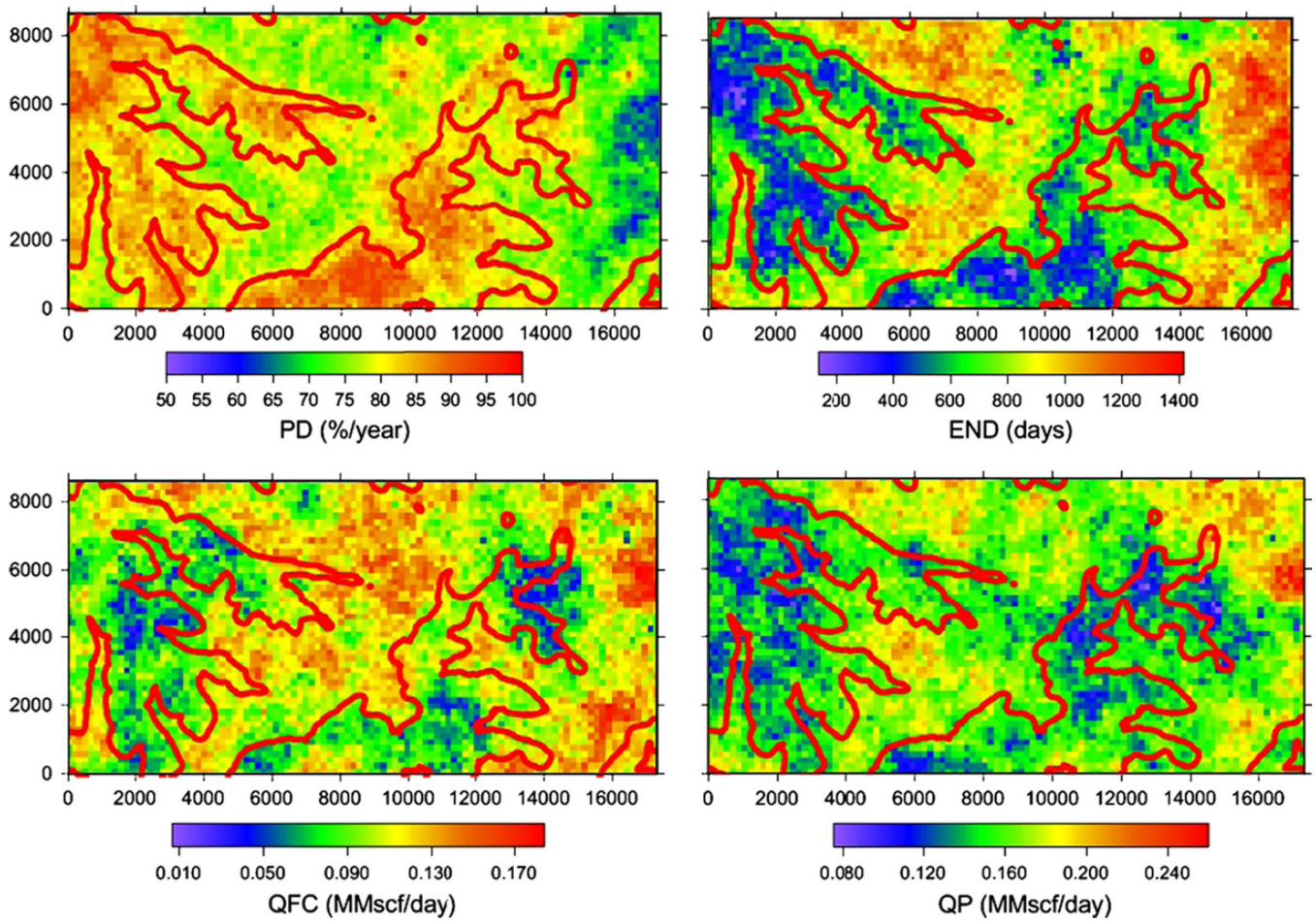

Fig. 13.

Q50 maps of percent decline (PD), production end time (END), methane rate at forecast start (QFC), and methane rate at production start (QP). The red line is the 1100-ft contour of surface elevation. (For interpretation of the references to color in this figure caption, the reader is referred to the web version of this article.)

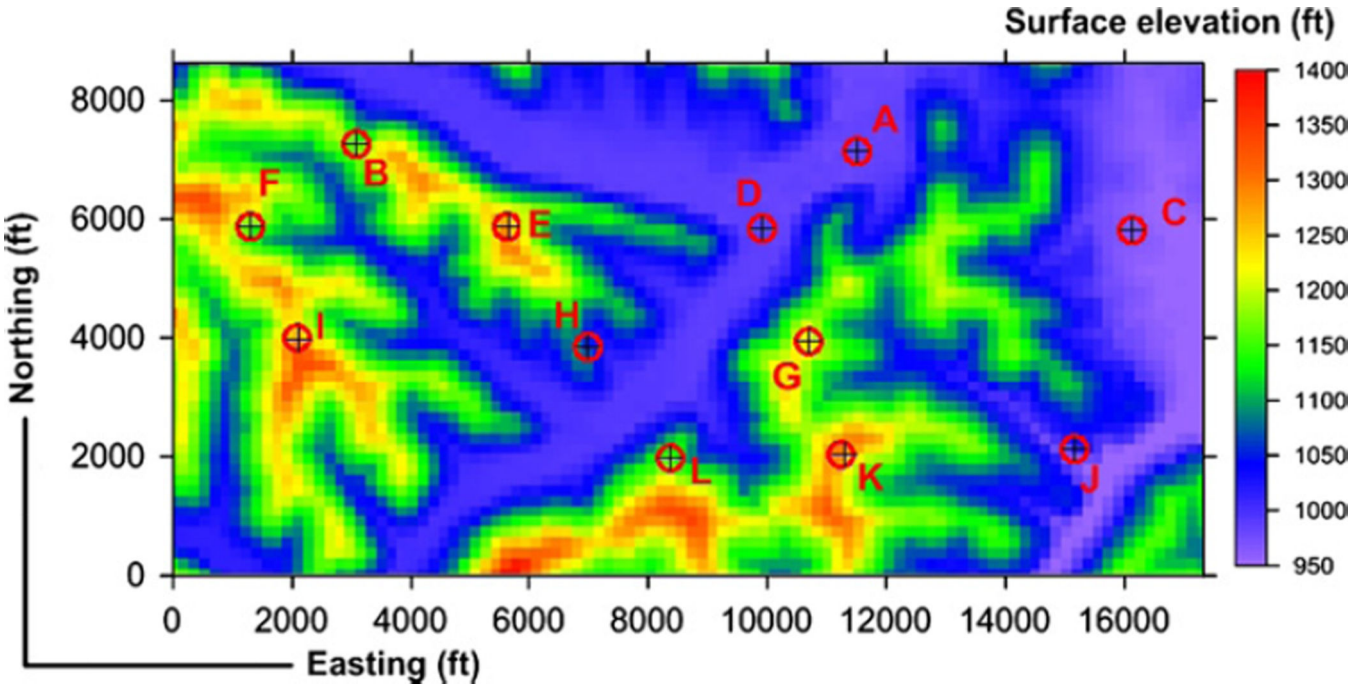

Fig. 14.
Virtual GGV locations to predict their performances.

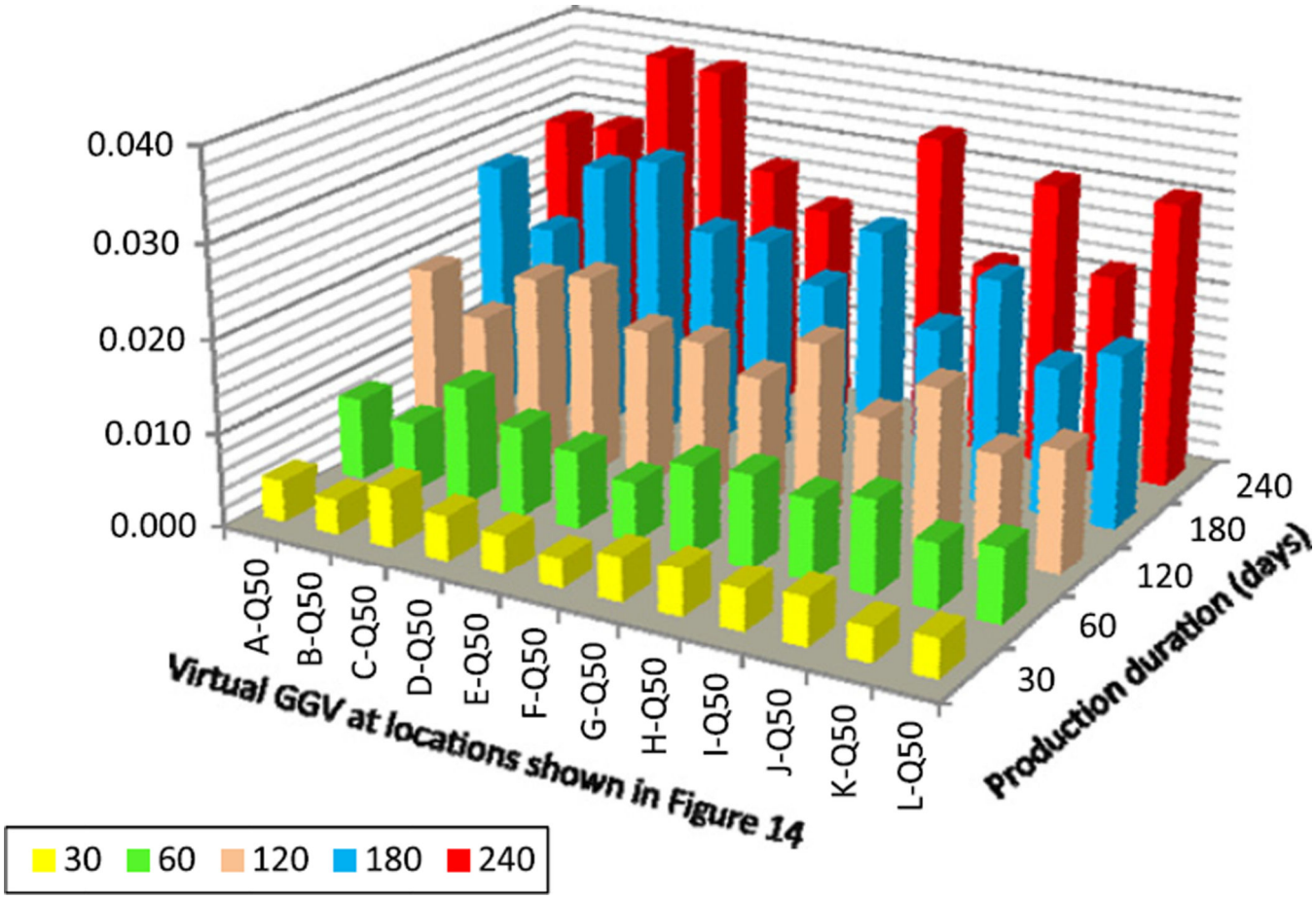

Fig. 15.

Cumulative production data (Q50) calculated using DCA maps and Eq. (2) for 30, 60, 90, 120, 180, and 240 days at the virtual GGV locations shown in Fig. 14.

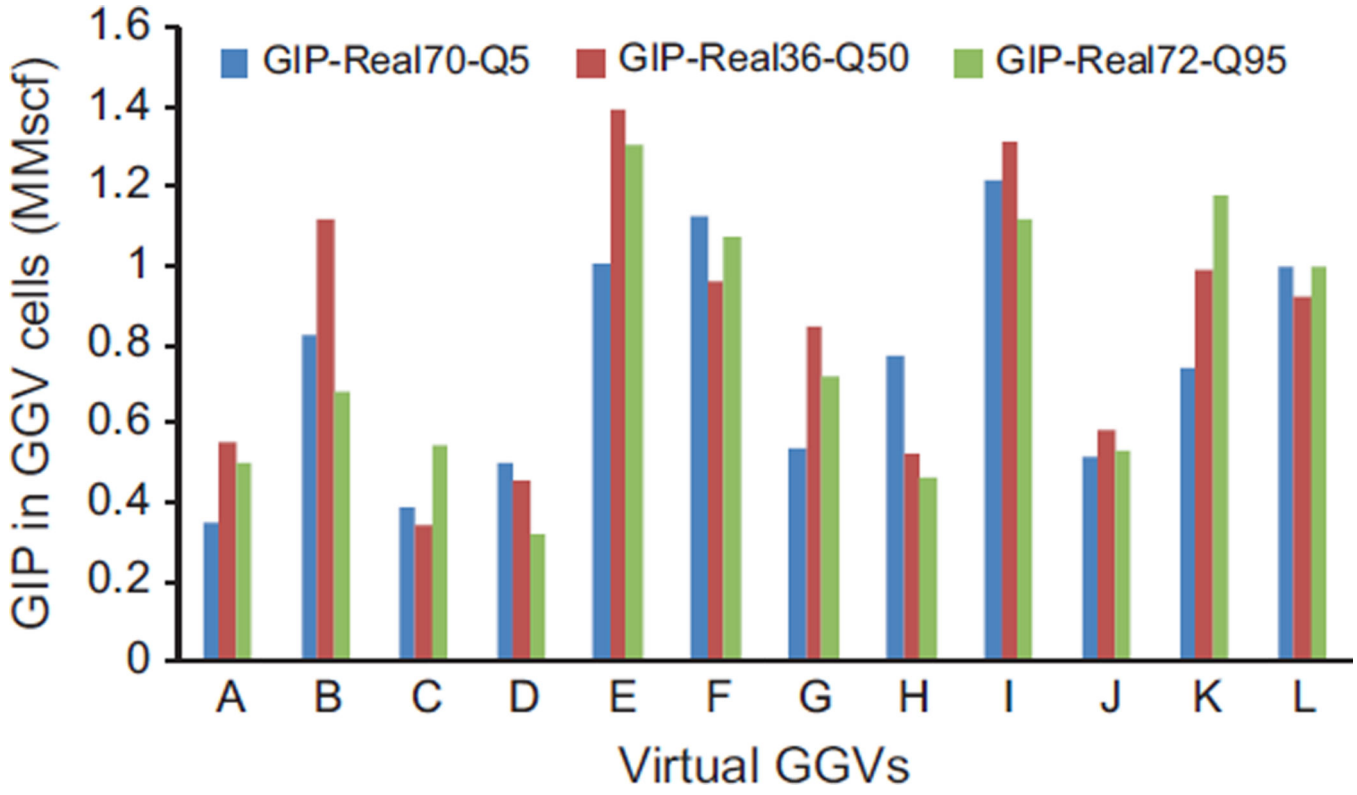

Fig. 16.
GIP amounts determined from Q5, Q50 and Q95 realizations for GGV locations shown in Fig. 14.

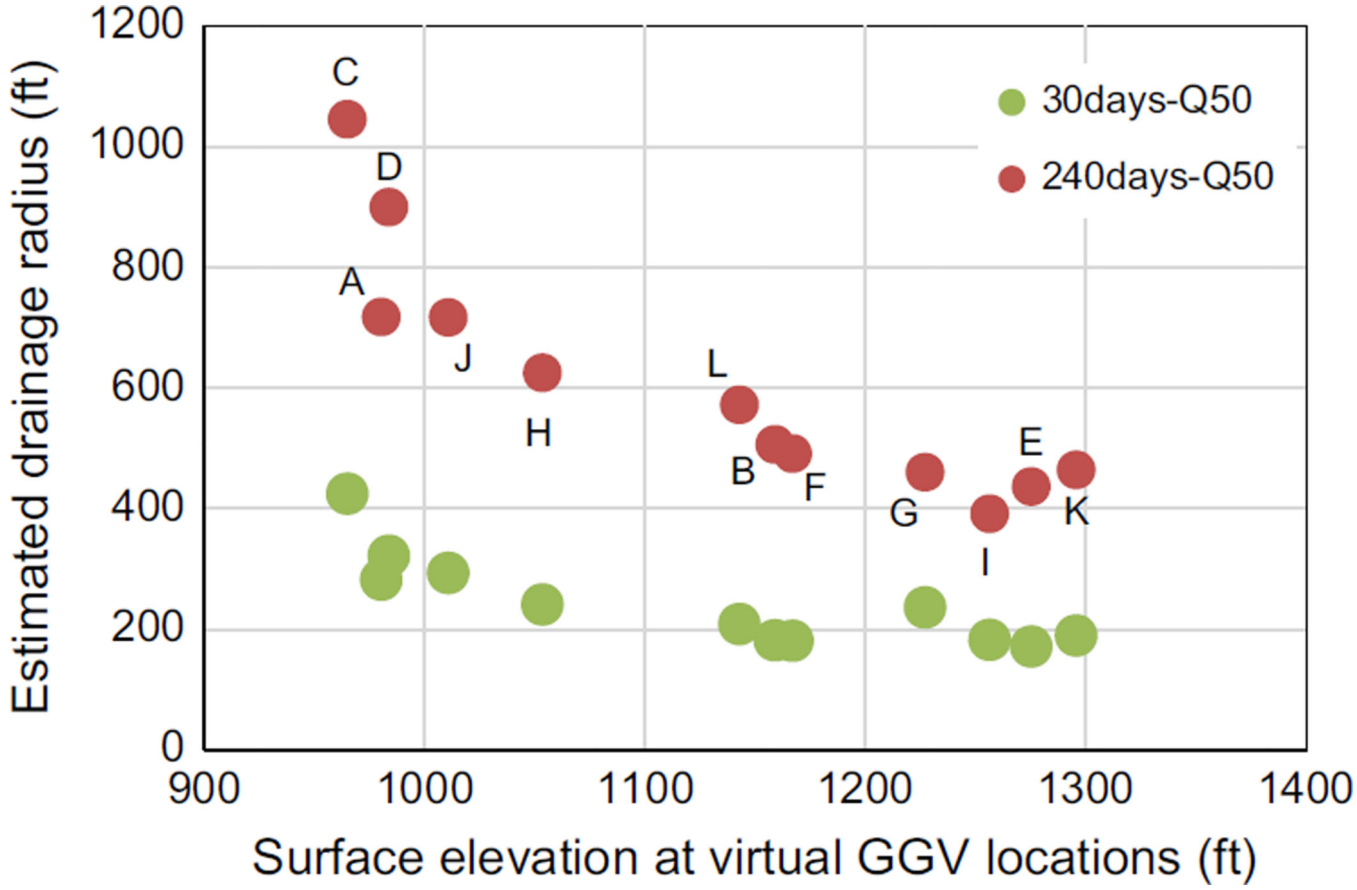

Fig. 17.

Drainage radius predictions as a function surface elevation using DCA and GIP results for GGVs drilled at virtual sample locations.

Table 1

Descriptive statistics of the DCA results of methane production data of GGVs.

Variable	# of observations	Min.	Max.	Mean	Std. *D*.
PD (%/year)	10	47.420	100.00	77.843	19.311
FC (days)	10	23.000	348.300	213.300	130.426
QFC (MMscf/day)	10	0.002	0.217	0.106	0.069
QP (MMscf/day)	10	0.002	0.336	0.162	0.096
END (days)	10	53.000	2517.000	793.350	772.359
CUM.P (Bscf)	10	0.003	0.102	0.043	0.030
EUR (Bscf)	10	0.005	0.172	0.068	0.051
RR (Bscf)	10	0.000	0.095	0.025	0.032

Table 2

Univariate statistical parameters of depth and thickness encountered by the exploration boreholes for Sewickley, Uniontown and Waynesburg coal seams.

Depth (ft)	Sewickley	Uniontown	Waynesburg
# of data	62	30	63
Mean	580.73	405.97	346.14
St. dev.	130.62	139.44	127.47
Variance	17,061.35	19,443.67	16,247.78
Minimum	341.73	192.70	103.60
Maximum	803.79	641.00	569.15
Thickness (ft)			
# of data	62	30	63
Mean	3.50	0.27	5.37
St. Dev.	1.994	0.088	0.585
Variance	3.979	0.008	0.343
Minimum	0.33	0.10	3.60
Maximum	6.90	0.50	6.99

Table 3

Summary of parameters that describe analytical semivariograms for depth and thickness attributes of Sewickley, Uniontown and Waynesburg coal seams, which were used to calculate GIP, and surface elevation. All semivariograms were analyzed using normal-score data and described with one-nested structure (model).

Depth (ft)	**Sewickley (SWC)**	**Uniontown coal (UNC)**	**Waynesburg (WBC)**	**Exploration boreholes**
Model	Spherical	Exponential	Exponential	
Nugget	0.1	0.1	0.1	
Sill	0.8	0.7	0.8	
Maximum range	3528	5400	4080	
Medium range	3384	5100	4020	
Minimum range	3168	4950	3780	
Thickness (ft)	Sewickley (SWC)	Uniontown coal (UNC)	Waynesburg (WBC)	Surface elevation (ft)
Model	Spherical	Gaussian	Spherical	Spherical
Nugget	0.1	0.07	0.3	0.1
Sill	0.5	0.95	0.6	0.9
Maximum range	5580	3850	3300	3872
Medium range	5580	3700	3150	3630
Minimum range	5580	3500	3075	3509

Table 4

Basic statistics of the histograms shown in Fig. 8.

Quantile	# of cells	Minimum (MMscf)	Maximum (MMscf)	Mean (MMscf)	Std. dev.
GIP- Q5	5000	0.242	1.433	0.728	0.268
GIP- Q50	5000	0.255	1.474	0.761	0.282
GIP- Q95	5000	0.253	1.404	0.790	0.274

Int J Rock Mech Min Sci (1997). Author manuscript; available in PMC 2015 July 15.

Table 5

Correlations between normal-score values of the DCA parameters with surface elevation data (NS refers to normal-score values). Description of variables is in the caption of Fig. 5. In this table, the correlations in red belong to the selected primary-secondary variable pairs. QP: initial production rate; FC: forecast start time; END: end of the potential production life of the well; PD: percentage decline (constant decline rate); QFC: rate at forecast start; CUM.P: cumulative production till forecast start; RR: recoverable reserves; EUR: expected ultimate recovery.

Variable*	**ELEV-NS**	**PD-NS**	**EUR-NS**	**END-NS**	**FC-NS**	**CUM.P-NS**	**RR-NS**	**QFC-NS**	**QP-NS**
ELEV-NS	**1**								
PD-NS	0.581	**1**							
EUR-NS	−0.443	−0.936	**1**						
END-NS	−0.710	−0.626	0.612	**1**					
FC-NS	−0.226	−0.521	0.696	0.754	**1**				
CUM.P-NS	−0.443	−0.936	**1.000**	0.612	0.696	**1**			
RR-NS	−0.553	−0.964	0.913	0.499	0.420	0.913	**1**		
QFC-NS	−0.466	−0.758	0.771	0.200	0.242	0.771	0.809	**1**	
QP-NS	−0.449	−0.820	0.868	0.362	0.474	0.868	0.884	0.929	**1**

Int J Rock Mech Min Sci (1997). Author manuscript; available in PMC 2015 July 15.

Table 6

Summary statistics of Q5, Q50, and Q95 realizations for DCA parameters. QP: initial production rate; END: end of the potential production life of the well; PD: percentage decline (constant decline rate); QFC: rate at forecast start (Real. stands for realization).

Variable/realization/quantile	# of cells	Min.	Max.	Mean	Std. Dev.
PD-Real96-Q5 (%/year)	5000	59.66	94.07	77.62	5.48
PD-Real32-Q50 (%/year)	5000	59.66	94.07	78.40	5.84
PD-Real63-Q95 (%/year)	5000	59.66	94.07	79.03	5.90
END-Real90-Q5 (days)	5000	132.72	1416.09	730.51	215.47
END-Real6-Q50 (days)	5000	132.72	1416.09	759.38	212.32
END-Real18-Q95 (days)	5000	132.90	1416.09	775.52	216.95
QFC-Real45-Q5 (MMscf/day)	5000	0.007	0.184	0.096	0.032
QFC-Real21-Q50 (MMscf/day)	5000	0.007	0.184	0.103	0.026
QFC-Real1-Q95 (MMscf/day)	5000	0.007	0.184	0.109	0.028
QP-Real38-Q5 (MMscf/day)	5000	0.075	0.260	0.153	0.027
QP-Real20-Q50 (MMscf/day)	5000	0.075	0.260	0.158	0.023
QP-Real34-Q95 (MMscf/day)	5000	0.075	0.260	0.162	0.027